UNIVERSIDADE DE COIMBRA
FACULDADE DE CIÊNCIAS E TECNOLOGIA
DEPARTAMENTO DE ENGENHARIA INFORMÁTICA

The role of 18F-FDG PET/CT in staging Breast Cancer

Comparative analysis with breast MRI

Joana Cristo dos Santos

Mestrado Integrado em Engenharia Biomédica

Supervisors:
Pedro Henriques Abreu
Inês Domingues

2018/2019

Abstract

Breast cancer is one of the main causes of mortality in women worldwide. Diagnosing is an important step that allows an early detection of the disease, which increases the chances of survival and the efficiency of the treatment.

Staging Breast Cancer is a complex process in which several imaging modalities are fundamental, such as Echography, Mammography, MRI, Bone Scintigraphy, PET/CT and CAT scan. Although PET/CT and MRI are not considered conventional methods for staging breast cancer, they provide essential information to evaluate this disease.

The main objective of this thesis is to develop an approach that can semi-automatically detect the primary site of breast cancer using two imaging modalities: whole-body PET/CT and breast MRI. To achieve this goal, a multi-step approach for each modality was developed based on image processing techniques, tested over a database of 143 breast cancer patients collected from IPO-Porto. The developed algorithms are divided into breast tissue identification and lesion detection, in which image processing techniques such as thresholding, co-registration, superpixels and clustering were applied.

The best approach was achieved through the tumor detection in PET/CT images, achieving an intersection over union of 0.308, a precision of 0.371, a recall of 0.568 and 2.766 false positives per patient. These results seem promising, however, future work must be implemented to increase the accuracy of the algorithm and improve the overall performance.

Keywords: Breast Cancer, Breast Cancer Diagnosis, Breast Cancer Staging, Image Processing, Imaging Techniques, PET/CT, MRI

Resumo

O cancro da mama é uma das principais causas de morte de mulheres no mundo. O diagnóstico é um passo importante que permite uma deteção precoce da doença, o que aumenta as probabilidades de sobrevivência e a eficácia do tratamento.

O estadiamento do cancro da mama é um processo complexo no qual várias modalidades de imagiologia são fundamentais, como por exemplo a Ecografia, a Mamografia, a RMI, a Cintigrafia Óssea, a PET/CT e o TAC. Apesar da PET/CT e da RMI não serem considerados métodos convencionais para o estadiamento do cancro da mama, estes providenciam informação essencial para avaliar a doença.

O principal objetivo desta tese é o desenvolvimento de uma abordagem que consegue semi-automaticamente detetar a localização primário do cancro da mama usando duas modalidades de imagiologia: PET/CT de corpo inteiro e RMI da mama. Para atingir esta meta, uma abordagem de vários passos para cada modalidade foi desenvolvida baseando se em técnicas de processamento de imagem, testada numa base de dados de 143 pacientes de cancro da mama recolhidos no IPO do Porto. O desenvolvimento do algoritmo é dividido na identificação do tecido mamário e na deteção da lesão, no qual técnicas de processamento de imagem como thresholding, co-registo, superpixels e clustering foram aplicadas.

A melhor abordagem foi obtida pela deteção do tumor em imagens PET/CT, obtendo um valor de 0.308 de interseção sobre união, de 0.371 de precisão, de 0.568 de recall e de 2.766 falsos positivos por paciente. Estes resultados são promissores, no entanto, trabalho futuro deve de ser implementado para aumentar a acurácia do algoritmo e melhorar a performance.

Palavras-Chave: Cancro da mama, Diagnóstico do cancro da mama, Estadiamento do cancro da mama, Processamento de imagem, Técnicas de imagiologia, PET/CT, MRI

Acknowledgments

I would like to express my sincere gratitude to my advisors Professor Pedro Henriques Abreu and Inês Domingues for the unconditional support, encouragement and useful critiques.

I would like to thank the medical team of IPO-Porto, especially Doctor Hugo Duarte, for the availability and cooperation.

I must thank Miriam Santos, for the availability and insightful comments.

I would like to thank all my friends and laboratory colleagues for motivation and support.

Finally, I would like to thank my family: my parents, cousins, and brothers, for making it possible.

Contents

Acronyms **xi**

List of Figures **xiv**

List of Tables **xvi**

1 Introduction **1**
1.1 Contextualization 1
1.2 Objectives 3
1.3 Document Structure 4

2 Background Knowledge **5**
2.1 Medical Imaging Modalities 5
2.1.1 PET/CT 5
2.1.2 MRI 6
2.2 Image Processing 7
2.3 Evaluation Metrics 8
2.3.1 Intersection over Union 9
2.3.2 True Positives, True Negatives and False Positives 10
2.3.3 Precision and Recall 10
2.3.4 Distance between the centroids of the Bounding Boxes 11

3 Literature Review **13**
3.1 Segmentation, Detection and Classification of Breast Cancer 13
3.2 Image Processing for medical image analysis: PET/CT and MRI 17
3.2.1 PET/CT images 18
3.2.2 MRI 20

4 Experimental Setup **23**
4.1 Data Collection 23
4.1.1 Data Organization 24

4.1.2 Subset of Data Selected . . . 24
4.1.3 Subset Characterization . . . 25
4.2 Analysis of PET/CT . . . 28
4.2.1 Pre-Processing . . . 28
4.2.2 Identification of the breasts . . . 31
4.2.3 Lesion Detection . . . 36
4.2.4 FP Reduction . . . 37
4.3 Analysis of MRI . . . 37
4.3.1 Pre-Processing . . . 37
4.3.2 Identification of the breasts . . . 39
4.3.3 Lesion Detection . . . 41
4.4 Challenges in the Development of the Algorithms . . . 43
4.4.1 Main Challenges in PET . . . 43
4.4.2 Main Challenges in MRI . . . 45
4.5 Experimental Results . . . 45
4.5.1 PET Results . . . 46
4.5.2 MRI Results . . . 47
4.5.3 Comparing PET with MRI . . . 48

5 Conclusions and Future Work **51**

Bibliography **53**

Acronyms

AC Attenuation Corrected

ASD Average Surface Distance

AUC Area Under the Curve

BC Breast Cancer

BL Bladder

BQML Becquerels/Millimeter

BR Brain

BRATS Brain Tumor Segmentation Challenge 2013 Database

CAD Computer-aided Diagnosis

CERR Computational Environment for Radiological Research

CFSC Class-driven Feature Selection and a Classification Model

CNN Convolutional Neural Networks

ConvNets Multi-view Convolutional Networks

CT Computer Tomography

CTV Clinical Target Volume

DB Database

DCE Dynamic Contrast-Enhanced

DDCNN Deep Dilated Convolutional Neural Network

DDNN Deep Deconvolutional Neural Network

DICOM Digital Imaging and Communications in Medicine

DSC Dice Similarity Coefficient

DWI Diffusion-Weighted Imaging

EER Early Enhancement Rate

EM Expectation-maximization

FATSAT Fat Saturation

FDG Fluorodeoxyglucose

FFS Feet First-Supine

FN False Negative

FNF False Negative Fraction

FP False Positive

FPF False Positive Fraction

H&N Head and Neck

HD Hausdorff distance

HE Heart

HFS Head First-Supine

HGG High Grade Gliomas

HY Other Hypermetabolic

IOU Intersection over Union

IPO Instituto Português de Oncologia

LDCT Low-dose Chest CT

LGG Low Grade Gliomas

LIDC-IDRI Lung Image Database Consortium

LK Left Kidney

MAD Mean Absolute Difference

MIP Maximum Intensity Projection

MLACMLS Maximum Likelihood Active Contour Model using Level Set

MRI Magnetic Resonance Imaging

MSE Multi-scale Superpixel-based Encoding

NAC Non-Attenuation Corrected

PCNN Pulse Coupled Neural Networks

PET Positron Emission Tomography

PET-AS PET Automatic Segmentation

PET/CT Positron Emission Tomography/Computer Tomography

PPV Positive Predictive Value

RFM Radiomic Feature Maps

RK Right Kidney

ROI Regions of Interest

RVD Relative Volume Difference

SBGFRLS Selective Binary and Gaussian Filtering Regularized Level Set

sFEPU Sites of normal FDG excretion and physiologic uptake

SLIC Simple Linear Iterative Clustering

SPF Signed Pressure Function

SPNs Solitary Pulmonary Nodules

SUV Standardized Uptake Value

SVM Support Vector Machine

T1-W T1-Weighted

T2-W T2-Weighted

TN True Negative

TP True Positive

List of Figures

2.1 Imaging modalities: PET, CT and MRI 7
2.2 Approaches for IOU calculation 9

4.1 PET/CT Methodology 23
4.2 PET Ground Truth Acquisition 27
4.3 MRI Ground Truth Acquisition 27
4.4 Different tissue signal characteristics in T1-W, T2-W and Contrast-Enhanced MRI 28
4.5 Analysis of PET/CT 29
4.6 Final 3D volume in PET 30
4.7 Positioning of body of the patient in PET 30
4.8 Identification of the breast tissue 31
4.9 Binary Masks: Frontal and Lateral MIP 32
4.10 Maximum Intensity Projection and Binary Mask: Frontal Perspective 33
4.11 Defining the Upper Limit 34
4.12 Defining the Lower Limit 34
4.13 Template Matching Method 36
4.14 Analysis of MRI 38
4.15 Final 3D volume in MRI 38
4.16 Positioning of body of the patient in MRI 39
4.17 Identification of the breast tissue 39
4.18 Background Elimination in MRI 40
4.19 Landmark Points Positioning in MRI 40
4.20 Elimination of the organs in MRI 41
4.21 Separation of the tissues in the breast 42
4.22 Separation of the K-means Clusters 43
4.23 Identification of the Tumor Cluster 44

List of Tables

2.1 Confusion Matrix 10

3.1 Main topics of the research projects related to BC 17
3.2 Main topics of the research projects related to PET/CT Segmentation 19
3.3 Main topics of the research projects related to PET/CT detection 20
3.4 Main topics of the research projects related to FP reduction 21
3.5 Main topics of the research projects related to MRI Segmentation 22

4.1 Each Modality in the Database 24
4.2 Components present in each MRI exam in the Subset Database. 26
4.3 Matches in the PET approach 46
4.4 Evaluation Metrics Values in the PET approach 46
4.5 Matches in the MRI approach 47
4.6 Evaluation Metrics Values for MRI 48

Chapter 1

Introduction

Breast Cancer (BC) was the second cancer with the highest incidence and the fifth cancer with the highest mortality rate in the year 2018 worldwide [1]. In the United States, BC is considered one of the most common cancers in women, representing 30% of all new diagnoses, and is estimated that in 2019, 268,600 new cases and 41,760 new deaths in the female population will occur [2].

With the evolution of technology and the development of new treatments, the mortality rate of BC has been decreasing but the incidence rate is still increasing worldwide [1]. To attenuate this phenomenon, a continuous development of new diagnosis methods and treatment techniques is required.

Medical imaging is a method used to diagnose and stage cancer. This thesis is focused on the development of a Computer-aided Diagnosis (CAD) system that detects the primary site of the BC in different types of imagiology based on image processing techniques.

1.1 Contextualization

BC affects mainly women older than 50 years. Screening campaigns and physical examination are essential prevention measures that increase the possibility of early detection and improve treatment efficiency [3]. BC treatment is mainly composed of the following steps: Diagnosis, Staging and Treatment with Evaluation of Response [4].

The diagnosis is commonly performed by mammography or physical examination. This is the first step in the process and is important to detect the tumor in an early stage of development.

In the staging phase, the physician evaluates the full extension of the disease and chooses the most appropriate treatment for each patient. To perform the staging, it is required to gather all the information associated with the state of the disease divided into three parts: Primary Site, Loco-regional and Distant (Systemic) [4]. The first part requires a full study of the breast tissue and the detection of all the lesions present in the mammary gland. This process allows

the identification and characterization of the primary site. The second part is Loco-regional Staging, corresponding to a full study of the regional lymph nodes. The breast tissue is located in close contact with the lymphatic system through regional lymph nodes located in the axilla, internal mammary, supraclavicular and intramammary areas. These are the main routes for the lymphatics drain from the breast and are the most likely primary metastization sites. The third part is Distant or Systematic Metastases Staging. The dissemination of tumour cells might happen through blood or lymphatic vascular systems. Due to the proximity of the breast tissue to a lymphatic drain, BC has a high probability to generate distant metastases. The main sites of metastization are bone, lungs, and liver [5]. After the staging process, a treatment approach is chosen and further evaluation of the response of the treatment is necessary. The correct staging leads to a better choice of treatment and an increase in the survival probability.

Imaging plays an important role in all the steps described above. Different imaging modalities provide different types of information and play distinct roles in each of these steps:

- **Mammography** - Essential for the examination of the breast tissue and very useful in the diagnosis phase due to its low price and easy acquisition protocols. However, even though this imaging method is commonly used, it might not be able to identify all lesions and in case of a positive result (suspicious or malignant mass is detected) other imaging modalities need to be performed;
- **Echography** - This method is further used in the staging phase and is a complementary imaging method to characterize the primary site and the regional lymph nodes;
- **CT Scan** - Thorax Computer Tomography (CT) Scan is used to identify possible metastases in the bone and lung tissue;
- **Bone Scintigraphy** - Since bone is one of the main metastization sites for BC, this modality allows a full body analysis of all skeletal system;
- **PET/CT** - Even though the format of lesions and their localization is essential, with full body PET/CT it is possible to anatomically identify the lesions and analyze how they behave metabolically as well. This image is a result of the co-registration between two modalities: Positron Emission Tomography (PET) and Computer Tomography (CT), integrating functional imaging from PET with anatomical imaging from CT;
- **MRI** - Breast Magnetic Resonance Imaging (MRI) allows the study of breast lesions and regional lymph nodes with more detail due to its high spatial resolution.

PET/CT and MRI are not considered conventional methods used for staging BC, however, those modalities have shown to provide crucial information to evaluate the disease [6]. PET/CT allows the physician to visualize the metabolic information through PET complemented by the morphology and the localization of the lesion through CT. Besides providing this dual information,

since it is a full-body image, it can also provide information about distant metastases that do not show in other types of modalities. MRI has a high spatial definition, ideal to detect smaller tumors and illustrate the morphology of a lesion which is essential to determinate its malignancy. This propriety is necessary when considering regional lymph nodes and tumors of small dimensions.

The main challenges in staging BC is the localization of a lesion in each image and the differentiation of the lesions between three categories: the primary site, regional lymph nodes, and distance metastases. This process is very time consuming and requires a physicians to manually annotate each lesion. Besides the identification of the lesions, due to the high cost of each exam, it is necessary to study the efficiency of each exam to verify if only one or all are necessary to perform the staging of the disease.

Due to these problems, new solutions must be found to decrease time and costs. Over the years, machine learning techniques have been used alleviate this issue [7, 8, 9, 10]. However, there is the need to improve medical imaging segmentation and the accuracy of detection and classification in BC patients.

1.2 Objectives

The main goal of this thesis is to develop an approach that can semi-automatically detect the primary site of the BC and analyze the effectiveness of each modality for staging the Primary Site.

The development of algorithms will be primarily focused on the study of PET/CT images, due to the versatility of the metabolic information provided by PET, which makes the information of these images different from all the other modalities. Afterwards, the detection in PET/CT is going to be compared with the detection in another modality, MRI. Bone Scintigraphy was considered for this comparison, however due to time restrictions and the number of patients that performed the imaging modality (representation of the modality in the collected data), MRI was selected.

In order to accomplish this main goal, a set of sub-tasks were defined:

1. **Collection of the data:** For this work, during a period of four months, real BC Patients data was collected from IPO-Porto. The patient information was composed by all imaging modalities (Mammography, Echography, CT Scan, Bone Scintigraphy, PET/CT and MRI) used during the staging process and corresponding medical reports;

2. **Selection of the modality to compare with PET/CT:** In an initial phase, several modalities were considered such as MRI and Bone Scintigraphy. MRI was chosen due to the representation of the modality in the collected Data (full justification is given in Section 4.1.2);

3. **Development of an approach to detect the primary site:** For each modality it is necessary the identification of the breast tissue and detection of existing lesions. The approach was implemented in MATLAB code;

4. **Evaluation of the detections:** After obtaining the detection of the lesions, a comparison is performed using the Ground Truth (full details are given in Section 4.1.3.3) and other metrics such as Intersection over Union, Precision, Recall and Distance between the centroids.

1.3 Document Structure

The structure of the document is organized as follows: in Chapter 2, Background Knowledge that helps the comprehension of the components of this work is presented; in Chapter 3, a Literature Review is performed to analyze the state-of-art methods used in the field of medical imaging; in Chapter 4, the applied methodology is described and the obtained results are presented; and finally, in Chapter 5, the conclusions and future work are summarized.

Chapter 2

Background Knowledge

In this chapter, theoretical background knowledge is presented in order to understand important concepts discussed throughout the document. The main topics reviewed correspond to the description of the imagiology modalities, imaging processing methods and the metrics used to evaluate the developed methods.

2.1 Medical Imaging Modalities

A Medical Imaging Modality is an imaging technique that uses a physical phenomenon to study the anatomical structure and/or the metabolic features of the human body. These techniques are noninvasive methods and are essential in a clinical setting. The imaging modalities used in this work, PET/CT and MRI are described below and illustrated in Figure 2.1.

2.1.1 PET/CT

Positron Emission Tomography (PET) is a nuclear functional imaging technique developed to use radio-pharmaceuticals as molecular probes to image and measure biochemical processes [11]. This technique measures the distribution of compounds by counting the annihilation photons emitted by the positron emission.

Positrons, which are antimatter equal in mass but opposite in charge to an electron, are emitted from proton-rich nuclei. Depending on their energy, positrons travel an average distance before interacting with an electron. The electron and positron annihilate each other and produce two antiparallel 511-keV photons. Detector crystals are mounted in a stationary ring, and only the photons with energy equal to 511-keV reaching opposing crystals coincidentally are counted [12].

The radiopharmaceuticals used are compounds labeled with positron-emitting radioisotopes. Some of the most common radioisotopes are cyclotron-produced 11-C, 13-N, 15-O, and 18-F as well as generator-produced 68-Ga and 82-Rb [13]. Since tumour tissue consumes more glucose

than healthy tissue, a radiopharmaceutical that is a glicose analogue is able to be located in higher glucose consumption areas. Fluorodeoxyglucose (FDG) is one the most common tracers and is often labeled with 18F. FDG has a similar cellular uptake to glucose and can pass through the cellular membrane through the facilitated transport activated by the glucose transporters.

Computer Tomography (CT) is a structural imaging technique that uses an X-ray beam through the body and measures its attenuation. This technique uses a scanner that rotates the source and the detector around the patient acquiring images planes and reconstructing the data into a 3D image.

Positron Emission Tomography/Computer Tomography (PET/CT) is a full-body image that results from the co-registration between two modalities, PET and CT, in which CT provides additional anatomical resolution for the functional imaging provided by PET [14].

2.1.2 MRI

Magnetic Resonance Imaging (MRI) is an imaging technique that uses a strong magnetic field and radio waves to generate images of parts of the body. This method relies on the properties of spin of Hydrogen atoms present in water molecules to obtain images.

Balanced nucleus (same number of protons and neutrons) have zero spin, however nuclei, like Hydrogen, create a small magnetic field known as magnetic moment, that can be influenced by an external field. The application of an external magnetic field to an area of the body, causes the hydrogen atoms to precess around the direction of the field. If an eletromagnetic radiation (radiofrequency signal) is applied to the precessing nuclei at a particular frequency (the Larmor frequency), the nuclei will shift to align in a different direction. Instead of the random precession seen with an external field, the nuclei will spin in harmony. Once the eletromagnetic radiation is removed, the nuclei will realign to their magnetic moment in a process called relaxation. During relaxation, the nuclei loses energy by emitting eletromagnetic radiation. This response signal is measured and reconstructed to obtain a 3D image.

There are two processes of relaxation:

- T1 relaxation - the time required for the magnetic moment of the displaced nuclei to return to equilibrium;
- T2 relaxation - the time required for the response signal from a given tissue type to decay.

Each tissue has a different response and consequently, a different value in T1 and T2. To understand the constitution of each tissue, the images between T1 and T2 have to be compared.

Parameters of the MRI technique can be adjusted to change the weighting of the T1 and T2 relaxation times, thus allowing image contrast to be manipulated. A contrast is often used to detect malignant lesions that cannot be identified by T1 and T2, as well as fat suppression techniques [15].

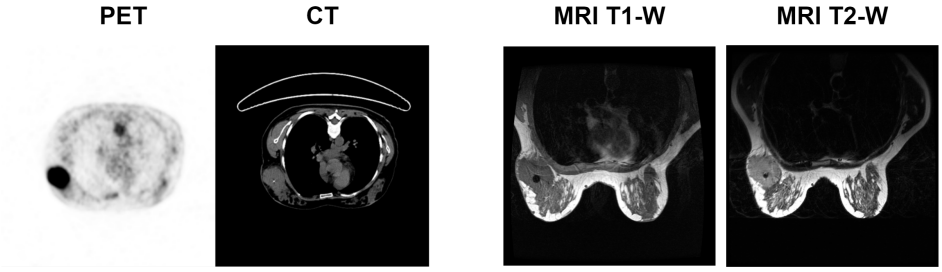

Figure 2.1: Illustration of the imaging modalities used in this work: PET, CT and MRI.

Other techniques that have been used to increase the resolution and the description of tumor characteristics of MRI are Dynamic Contrast-Enhanced (DCE)-Magnetic Resonance Imaging (MRI) and Diffusion-Weighted Imaging (DWI) [6]. acrshortdce-MRI is an exogenous contrast-based method that uses rapid and repeated T1-Weighted images to measure the signal changes induced by the paramagnetic tracer in the tissue as a function of time [16]. DWI is a MRI technique that is sensitive to the Brownian molecular motion of spins. Since the extent and orientation of molecular motion is influenced by the microscopic structure and organization of biological tissues, DWI can depict various pathological changes in organs or tissues [17].

2.2 Image Processing

Image Processing is an area of research that treats and analyses images. Two of the main fields in image processing are **image segmentation** and **image detection**.

Image Segmentation is the process of dividing an image into several Regions of Interest (ROI). Applied to Medical Imaging, image segmentation allows, for instance, the delimitation of different tissues and consequentially a more targeted analysis. The process of identification of the target tissue was not the main focus of this project, however its identification is the first step to perform the detection and thus, is important for better results in the detection phase.

Image Detection is the process of identifying certain structures in an image, considered ROI (for instance, abnormal structures in the tissue, such as lesions).

Due to the variability of the medical modalities studied, a few techniques of image processing were explored, such as [18]:

- **Threshold Techniques -** These techniques segment images by creating a binary partitioning of the image intensities using an intensity value, called threshold [18]. This approach is the simplest approach in imaging processing, however, is very effective to segment images with high contrasting intensities between ROI;

- **Detection of Peaks and Valleys -** This technique is based on the search of certain

characteristic areas, through lateral screening, such as maximum or minimum intensities, in order to detect points of interest;

- **Co-registration -** This technique is used to study different modality images and allows the alignment between the images. To apply this method, one of the images is considered fixed and the other suffers transformations (such as translations, rotations and scale modifications) in order to be aligned with the fixed image;

- **Template-based/Atlas-Guided Approach -** This approach uses a pre-existing template and treats the problem as a registration problem, in which the template is co-registered with the target image that requires segmentation;

- **Superpixels -** This method groups pixels into regions accordingly to pixels intensity using an algorithm called Simple Linear Iterative Clustering (SLIC) [19]. The application of this method reduces the complexity of subsequent image processing tasks. If this method is applied in a 3D approach, the regions originated are called Supervoxels;

- **Clustering -** This technique is used, in the present context, to reduce the number of Supervoxels originated by the SLIC algorithm. The Clustering method used is K-means, a type of unsupervised learning in which the volume is divided into k clusters of Supervoxels based on feature similarity [20].

- **False Positives Reduction -** This technique is applied to reduce the number of false detections obtained after the detection phase. To perform this technique, several methods can be used such as filters.

2.3 Evaluation Metrics

The evaluation of automatic techniques for detection depends on the type of problem and the type of data. In this work, the Ground Truth is composed by manually extracted bounding boxes surrounding the lesions in each modality.

The comparison between bounding boxes of the Detection and the Ground Truth is different from the attribution of a class to each pixel in an image. The evaluation of the detection using bounding boxes has no consensus in the best choice of metrics to use and there are several possible approaches to evaluate these types of problems. The metrics chosen for this work were selected due to the versatility of the results and their adaptation to a lesion detection problem. In this section, we describe the metrics that were used to evaluate this problem.

2.3.1 Intersection over Union

Intersection over Union (IOU) evaluates the overlap between two bounding boxes, A and B.

$$IOU = \frac{Volume\ of\ Intersection}{Volume\ of\ Union} = \frac{Volume(A \bigcap B)}{Volume(A \bigcup B)} \tag{2.1}$$

This metric has a value between 0 and 1, where 0 corresponds to a mismatch and 1 corresponds to a perfect match.

For evaluating IOU, two approaches were studied (Figure 2.2):

- **Approach 1 -** the value of IOU including all the bounding boxes from the Ground Truth and the Detection was calculated;
- **Approach 2 -** the average of the maximum values of IOU for the best match for each bounding box of the Ground Truth was calculated.

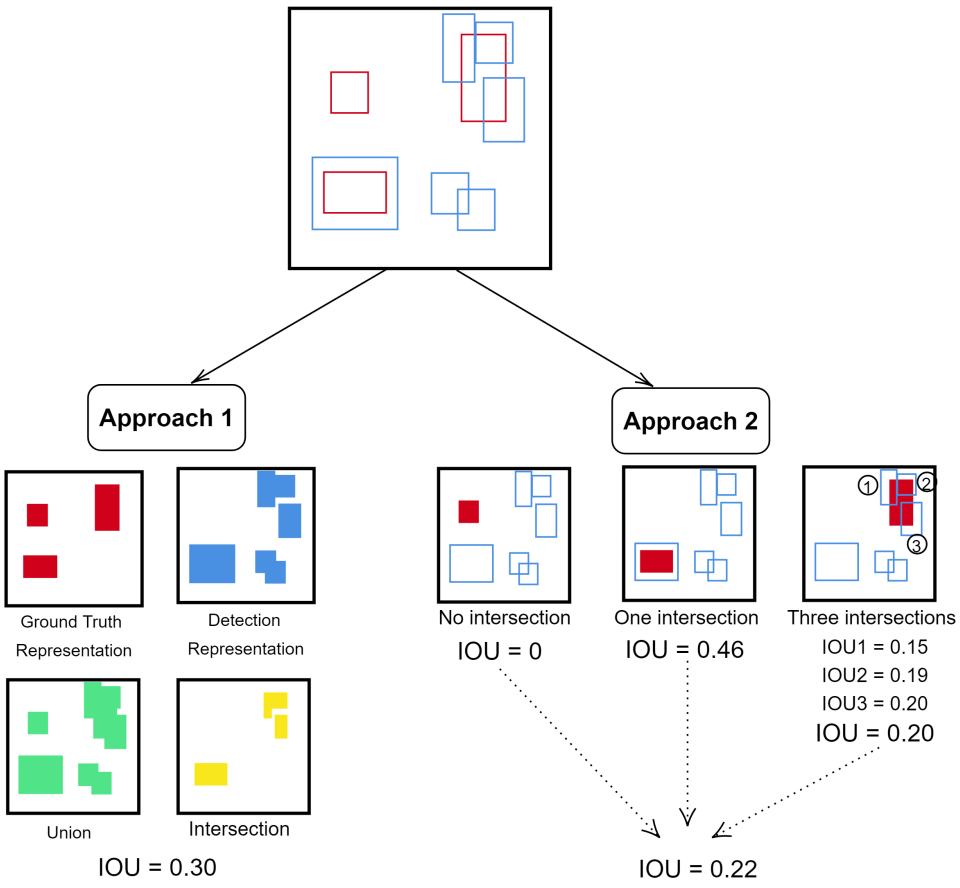

Figure 2.2: Diagram of the two approaches for IOU calculation in 2D. In the top image, the red bounding boxes correspond to the Ground Truth and the blue bounding boxes correspond to the Detection.

2.3.2 True Positives, True Negatives and False Positives

These metrics are usually defined based on a confusion matrix, by comparing the real versus the predicted classes (Table 2.1). However, in this case, since bounding boxes are compared, a few adaptations were performed. To define these parameters, the values of IOU between the Ground Truth and the Detection bounding box were considered, using the conditions:

- True Positive (TP) - True detection, is defined if IOU >= threshold;
- False Positive (FP) - False detection, is defined if IOU < threshold;
- False Negative (FN) - a ground truth bounding box that was not detected;
- True Negative (TN) - is not applied in this context.

Table 2.1: Representation of a Confusion Matrix for a binary class problem.

		Predicted Class	
		P	**N**
Actual Class	**P**	True Positives (TP)	False Negatives (FN)
	N	False Positives (FP)	True Negatives (TN)

The threshold used is important in the definition of the match considered a TP. Since we are working in 3D, the threshold considered should be different from the threshold used in 2D, which is typically 0.5. In order to produce similar results between the 2D and 3D approaches, similar precision-recall curves have to be defined. To achieve this condition, a threshold of 0.25 is chosen for the 3D approach [21].

2.3.3 Precision and Recall

Based on the values obtained in Section 2.3.2, a few evaluation metrics can be defined.

Precision measures the ability to identify the correct detections of relevant objects and can be calculated using:

$$Precision = \frac{TP}{TP + FP} \tag{2.2}$$

Recall measures the ability to identify all the correct detections of Ground Truth objects and can be calculated using:

$$Recall = \frac{TP}{TP + FN} \tag{2.3}$$

2.3.4 Distance between the centroids of the Bounding Boxes

The distance between the centroids of two bounding boxes, (x_A, y_A, z_A) and (x_B, y_B, z_B), is defined as the euclidean distance between a Ground Truth bounding box and a Detection bounding box, expressed in *millimeters (mm)*.

$$Distance = \sqrt{(x_A - x_B)^2 + (y_A - y_B)^2 + (z_A - z_B)^2} \tag{2.4}$$

The value considered to evaluate this metric is the average of the minimum values of distance between the centroids for each bounding box of the Ground Truth compared with all the Detection bounding boxes.

Chapter 3

Literature Review

In this chapter, a review of research work using machine learning techniques to perform image segmentation, detection and classification in PET/CT, PET, CT and MRI is presented.

3.1 Segmentation, Detection and Classification of Breast Cancer

BC segmentation, detection and classification are essential tasks to aid clinical professionals to evaluate the disease. These tasks are difficult to perform due to the localization of the disease, the variability of the imaging protocols and the composition of the tissues. For the past decades, Machine Learning techniques have been used to perform such tasks. Next, a list of BC works using such techniques will be described.

To help the reader follow the related work, a summary of the main topics related to works focused on BC is presented in Table 3.1.

Liu et al. [22] proposed a fully automated algorithm to segment the whole breast in Low-dose Chest CT (LDCT). This algorithm was developed based on an anatomy directed rule-based method. The evaluation of the algorithm was performed on 20 LDCT images from the LIDC public dataset. The ground truth for the breast region was manually annotated by a radiologist on one axial slice (at the axial level intersecting nipples) and two sagittal slices (at the median level of left and right breast). An analysis containing axial and sagittal slices, achieved an overall mean Dice Similarity Coefficient (DSC) of 0.880 with standard deviation of 0.058. However, the evaluation of the types of slices separately reports a mean DSC of 0.930 for axial slices and a mean of 0.830 for sagittal slices. As conclusion, the algorithm has a satisfactory determination of lateral, anterior, and posterior extents but suggests that the automatically determined vertical extents generally differ from the manually annotated extents.

Men et al. [23] aimed to train and evaluate a deep dilated residual network (DD-ResNet-101) for auto segmentation of the Clinical Target Volume (CTV) for BC radiotherapy with big data.

The method developed is a deep learning-based segmentation method, end-to-end segmentation framework that could predict pixel-wise class labels in CT images. The data used was extracted from early-stage BC patients who underwent breast-conserving therapy from January 2013 to December 2016 in the Department of radiation oncology from Cancer Hospital, Chinese Academy of Medical Sciences. In total, 57 878 CT slices were collected from 800 patients, in which 400 patients have right-sided BC and the other 400 have left-sided BC. Ground Truth segmentations were defined as the reference segmentation and cross-checked by experienced radiation oncologists. The original 2D CT images were the inputs and the corresponding CTV segmentation probability maps were the outputs. The performance of the proposed model was evaluated against two different deep learning models: Deep Dilated Convolutional Neural Network (DDCNN) and Deep Deconvolutional Neural Network (DDNN). Mean DSC values of DD-ResNet (0.91 and 0.91) were higher than the other two networks (DDCNN: 0.85 and 0.85; DDNN: 0.88 and 0.87) for both right-sided and left-sided BC. It also has smaller mean Hausdorff distance (HD) values of 10.5mm and 10.7mm compared with DDCNN (15.1mm and 15.6mm) and DDNN (13.5mm and 14.1 mm). Mean segmentation time was 4s, 21s and 15s per patient with DDCNN, DDNN and DD-ResNet, respectively. The proposed method could segment the CTV accurately with acceptable time consumption.

Liu et al. [24] proposed an approach for breast lesion segmentation from DCE-MRI using a level set-based active contour model. The model used the same principle as Selective Binary and Gaussian Filtering Regularized Level Set (SBGFRLS), controlled by a specially designed Signed Pressure Function (SPF) that only accounts for the distribution of image background intensity. The dataset used has a total of 38 breast DCE-MRI studies (29 malignant and 9 benign) acquired using the VIBRANT sequence in First Affiliated Hospital of Dalian Medical University. The ground truth to evaluate the accuracy of the proposed approach for each data was given by two medical experts. To confirm the proposed approach, a comparison is performed with C-V model, SBGFRLS and Maximum Likelihood Active Contour Model using Level Set (MLACMLS). The method has a Mean Absolute Difference (MAD) and Jaccard index of 7.256 ± 12.454 pixels and 0.86 ± 0.049 compared to the manual ground truth, while SBGFRLS has MAD and Jaccard of 19.341 ± 30.699 and 0.817 ± 0.128 and MLACLS 8.931 ± 15.964 and 0.856 ± 0.056. Compared with SBGFRLS, C-V and MLACMLS methods, this approach has a higher Jaccard index and lower MAD than the former two, which corresponds to a higher similarity between detection and ground truth .

Gubern-Mérida et al. [25] aimed to develop a method to automatically compute breast density in breast MRI. The framework is a combination of image processing techniques to segment breast and fibroglandular tissue. Three pre-processing algorithms are initially applied: correction of image inhomogeneities using the N3 bias field correction algorithm [26], sternum detection and the normalization of the intensities of the MRI to compensate for inter-patient signal intensity variability. In the breast segmentation step, the breasts are identified as the

region delimited by the breast-body surface determined by segmenting body structures using an atlas-based voxel classification algorithm and the air-breast boundary defined by a region growing algorithm applied slice by slice. In the breast density segmentation step, the breast volume is first defined for each breast independently and the dense tissue is segmented using the Expectation-maximization (EM) algorithm independently on each breast. The algorithm is tested in a dataset composed by a random subset of 50 pre-contrast coronal T1-W MRI breast volumes from 50 patients, collected from 2003 to 2009. In order to evaluate the automatic breast segmentation algorithm and construct the atlas, 27 cases were manually segmented by a single experienced observer. For breast segmentation, the proposed approach obtained DSC, total overlap, False Negative Fraction (FNF), and False Positive Fraction (FPF) values of 0.94, 0.96, 0.04, and 0.07, respectively. For fibroglandular tissue segmentation, the approach obtained DSC, total overlap, FNF, and FPF values of 0.80, 0.85, 0.15, and 0.22, respectively. The results achieved show that the method is able to segment both tissues with high values of overlap associated with a low number of false detections.

Liang et al. [27] proposed an automated method to detect lesions to assist radiologists in interpreting DCE-MRI of breast. In this approach, the localization of the suspicious regions is obtained by applying thresholds on three features: subtraction intensity, enhancement integral and Early Enhancement Rate (EER). Support Vector Machine (SVM) classifier is then applied to exclude normal tissues from these regions, using both kinetic and morphological features (cumulative histogram of mean values of integral, EER, subtraction intensity, mean values of the regions and lesion volume). The dataset used is composed by 21 patients and a total of 50 lesions, that were segmented manually and then edited by a radiologist. A detected region is identified as a true lesion if the overlap with the ground truth is greater than 40%, otherwise it is considered a FP detection. In the initial detection phase, all 50 true lesions were detected, and 550 other normal regions were signalized as lesions. After the reduction of FPs, only 298 FPs were eliminated. The final result achieved 100% sensitivity in both initial and after FP reduction phases but with a cost of 5.04 FP per lesion.

Parekh and Jacobs [28] presented a radiomic feature mapping framework to generate radiomic MRI texture image representations called the Radiomic Feature Maps (RFM) and correlate the RFM with quantitative texture values, breast tissue biology using quantitative MRI and classification of benign or malignant tumors. The algorithm was tested on a retrospective cohort of 124 patients (26 benign and 98 malignant) who underwent multiparametric breast MRI at 3 T. The MRI parameters used were T1-W imaging, T2-W imaging, DCE-MRI and DWI. The RFM were computed by convolving MRI images with statistical filters based on first order statistic and gray level co-occurrence matrix features. A multi-view feature embedding method is implemented using the RFM and IsoSVM model [29] is trained using leave-one-out cross validation which resulted in sensitivity and specificity of 93 and 85%, with an Area Under the Curve (AUC) of 0.91 in classifying benign from malignant lesions.

Antropova et al. [30] proposed the use of Maximum Intensity Projection (MIP) images of subtraction MRI into lesion classification using convolutional neural networks (CNN). The dataset used was collected at the University of Chicago, from 2006 until 2016, and includes 690 breast cases, with 212 benign and 478 malignant cases based on pathology and radiology reports. The ROI were defined around each lesion on three MRI presentations: (i) the MIP image generated on the second post-contrast subtraction MRI, (ii) the central slice of the second postcontrast MRI, and (iii) the central slice of the second postcontrast subtraction MRI. CNN features were extracted from the ROI using pre-trained VGGNet. The features were utilized in the training of three SVM classifiers (one for each MRI presentation) to characterize lesions as malignant or benign. The approach using MIPs (AUC = 0.88) outperformed those using central slice of the second postcontrast MRI (AUC = 0.80) and using central slice of second postcontrast subtraction MRI (AUC = 0.84).

Hassanien and Kim [31] introduced an hybrid approach that combines fuzzy sets, Pulse Coupled Neural Networks (PCNN), and SVM, in conjunction with wavelet-based feature extraction, to classify BC images into two classes: normal or abnormal. The algorithm is composed by three fundamental phases: pre-processing (enhancement of the contrast of the whole image using fuzzy type-II algorithm, detection of the boundary of the breast region and enhancement of the edges surrounding the ROI using PCNN-based segmentation); feature extraction-based wavelet transform; and classification using SVM. The approach is tested in a dataset, acquired from patients with abnormal pathologies, containing 120 images, in which 70 are normal images and 50 are considered abnormal. The SVM technique was compared with other machine learning techniques including decision trees, rough sets, neural networks, and fuzzy artmap. The experimental results show that SVM (98% accuracy) was superior to the other machine learning techniques: rough sets (92%), decision tree (89.7%), Neural networks (91%) and fuzzy artmap (88%).

The works discussed above consider a wide range of algorithms possible to apply in BC context. In most of these research works, the dataset used was not available to the public and was collected from a Hospital where the images were acquired with the same imaging protocol. This approach allows the reduction of the errors associated with the variability of imaging protocols and types of acquisition machines.

The most commonly used imaging modality is MRI for the context of BC. This happens due to the fact that only in the recent years, PET/CT has been become an important tool in staging BC and consequently new machine learning approaches are appearing to aid the process. Even though PET/CT is not yet commonly used in the context of BC, it is already applied for other diseases.

All of theses article mention pixel-by-pixel detection or segmentation methods, in which the most common metric used is DSC. In a context of comparing bounding boxes, the metrics are different and adapted to the type of evaluation required.

Table 3.1: Main topics of the research projects related to BC revised in Section 3.1.

Authors	Objective	Dataset	Evaluation Metrics	Results
Liu et al. [22]	Segmentation	20 Low-Dose Chest CT	DSC	0.880 ± 0.058
Men et al. [23]	Segmentation	57 878 CT slices	DSC, HD	0.91 and 0.91, 10.5 and 10.7mm (for right and left)
Liu et al. [24]	Segmentation	39 DCE-MRI	MAD, Jaccard index	7.256±12.454, 0.856±0.049
Gubern-Mérida et al. [25]	Segmentation	50 pre-contrast coronal T1-W MRI	DSC, total overlap, FNF, FPF	Breast: 0.94, 0.96, 0.04, 0.07 Fibroglandular: 0.80, 0.85, 0.15, and 0.22
Liang et al. [27]	Detection	21 breast DCE-MRI	Sensitivity, FPs	100%, 5.04 per lesion
Parekh and Jacobs [28]	Classification	124 breast MRI (T1-W, T2-W, DCE-MRI and DWI)	Sensitivity, Specificity, AUC	93%, 85%, 0.91
Antropova et al. [30]	Classification	690 subtration breast MRI	AUC	0.88
Hassanien and Kim [31]	Classification	120 breast MRI	Accuracy	98%

Breast tissue segmentation is commonly performed using an atlas-based approach, however it is not considered the best method because it depends on the accuracy of the atlas. Liu et al. [22] developed a new approach based on anatomy based rules implemented in CT images. This method was able to segment the tissue in 2D and 3D, however, the evaluation performed shows that in 2D the results are satisfactory but not ideal for this problem, requiring a more complex analysis and a 3D evaluation.

Detection problems are often associated with a high number of FPs, which cause a low accuracy. To increase the efficiency of the algorithm, a posterior step to reduce the number of FPs is required [27].

Classifiers, in particular Neural Networks and Deep Learning techniques, are often used for the classification of lesions. So far, these methods focus in differentiating malignant from benign lesions [28, 30], however for each pathology other characteristics can be taken into consideration.

3.2 Image Processing for medical image analysis: PET/CT and MRI

In this section, new approaches applied in PET/CT and MRI to different pathologies are explored.

3.2.1 PET/CT images

Tumor Segmentation

To segment a tumor in PET, it is required to identify the normal active organs and to segment the tumor accordingly to its characteristics.

Berthon et al. [32] aimed to develop a segmentation model, trained to automatically select and apply the best PET Automatic Segmentation (PET-AS) method, according to the tumour characteristics. ATLAAS is an automatic decision tree-based learning algorithm for advanced segmentation. The model developed included nine PET-AS methods and was trained on a dataset generated using the PETSTEP simulator (CERR) based on existing PET/CT data of a fillable phantom. In total, 100 PET scans were generated with known true contours. A decision tree was built for each PET-AS algorithm to predict its accuracy, quantified using the DSC, according to the tumour volume, tumour peak to background SUV ratio and a regional texture metric. The performance of ATLAAS was evaluated for 85 PET scans obtained from fillable and printed subresolution sandwich Head and Neck (H&N) phantoms. ATLAAS showed excellent accuracy across a wide range of phantom data and predicted the best or near-best segmentation algorithm in 93% of cases. It outperformed all single PET Automatic Segmentation (PET-AS) methods on fillable phantom data with a DSC of 0.881 and on H&N phantom data with a DSC of 0.819, while the best performing PET-AS method achieved a DSC of 0.831.

Afshari et al. [33] proposed a deep learning method to localize and detect normal active organs visible in a 3D PET scan field-of-view. It is based on an adaption of the deep network architecture YOLO to detect multiple organs in 2D slices and aggregate the results to produce semantically labeled 3D bounding boxes. The architecture is modified to take as input coronal 2D PET slices and to detect up to 5 different organ classes: brain, heart, bladder, and left and right kidneys. The dataset used is composed by 479 18F-FDG PET scans of 156 patients from the public collection of head and neck cancer from the Quantitative Imaging Network of the US National Cancer Institutes. The 479 scans were split as follows: 79 patients were used for training; and the other 77 patients were used for testing. The results show that the approach achieved an average organ detection precision of 75-98%, recall of 94-100%, average bounding box centroid localization error of less than 14 mm, wall localization error of less than 24 mm and a mean IOU of up to 72%.

In Table 3.2, a summary of the main topics of the described works on PET/CT Segmentation are presented.

Image Detection

Image Detection in PET/CT deals with problems characteristic to the modalities incorporated, such as the comprehension of FDG uptake in PET and the integration between the information collected from PET and CT.

Bi et al. [34] aimed to solve the problem correlated with the incorrect identification of Sites

Table 3.2: Main topics of the research projects related to PET/CT Segmentation.

Authors	Target Tissue	Dataset	Evaluation Metrics	Results
Berthon et al. [32]	Pulmonary Nodules	100 PET scans generated for training and 85 PET scans obtained for evaluation from phantoms	DSC	0.881
Afshari et al. [33]	5 organs: brain, heart, blandder, and left and right kidneys	479 18F-FDG PET/CT from 156 patients: 79 for training and 77 for testing	Precision, Bounding box centroid localization error, Wall localization error and IOU	75-98%, 14mm, 24mm and 72%

of normal FDG excretion and physiologic uptake (sFEPU), that happens in organs as kidneys, bladder, brain and heart. The proposed algorithm uses a Multi-scale Superpixel-based Encoding (MSE) to group the individual sFEPU fragments into large regions, a Class-driven Feature Selection and a Classification Model (CFSC) for sFEPU classification. The different sFEPU fragments are classified into Brain (BR), Bladder (BL), Heart (HE), Left Kidney (LK), Right Kidney (RK), and Other Hypermetabolic (HY). The algorithm was tested in a dataset consisting of 40 whole-body PET/CT from 11 lymphoma patients provided by the Department of Molecular Imaging, Royal Prince Alfred Hospital, Sydney. The experiments performed using this method achieved an average F-score of 91.73%, compared to the algorithms: SP-SD - sFEPU classification via multi-scale superpixels with sparse and dense representations (F-score of 90.10%); Grouping - a clustering based classification method (F-score of 82.36%); and Patch-SVM - multi-scale sliding window with SVM (F-score of 85.34%).

Zhao et al. [35] proposes a method that combines the features of PET and CT to detect and classify Solitary Pulmonary Nodules (SPNs) with few FPs. Initially, the algorithm uses a dynamic threshold segmentation method to identify lung parenchyma in CT images and suspicious areas in PET images. Then, an improved watershed method was used to mark suspicious areas on the CT image. Next, the SVM method was used to classify SPNs based on textural features of CT images and metabolic features of PET images to validate the proposed method. The dataset used is composed by 219 patients, 120 patients with SPNs and the remaining 99 patients had inflammation, collected from January 2010 to January 2013 at the Coal Center Hospital in Shanxi. This method was more efficient than traditional methods and methods based on the CT or PET features alone, achieving sensitivity of 95.6% and an average of 2.9 FPs per scan.

In Table 3.3, a summary of the main topics of the described works on PET/CT Detection are presented.

Reduction of False Positives

Besides detecting possible candidates as lesions, one of the main concerns for the developed algorithms is the high percentage of originated FPs.

Teramoto et al. [36] proposed an improved FP-reduction method to detect pulmonary nodules

Table 3.3: Main topics of the research projects related to PET/CT detection.

Authors	Target Tissue	Dataset	Evaluation Metrics	Results
Bi et al. [34]	6 fragments: brain, bladder, heart, left and right kidneys and other hypermetabolic	40 whole-body PET/CT from 11 patients	F-score	91.73%
Zhao et al. [35]	Solitary Pulmonary Nodules (SPNs)	219 whole-body PET/CT collected from 2011 to 2013	Sensitivity, FPs	95.6% 2.9 per scan

in PET/CT images using Convolutional Neural Networks (CNN). First, initial nodule candidates were identified separately on the PET and CT images using the algorithm specific to each image type, in PET a threshold method and in CT an active contour filter. Subsequently, candidate regions obtained from the two images were combined. FPs contained in the initial candidates were eliminated by an ensemble method using multistep classifiers on characteristic features obtained by a shape/metabolic analysis and a CNN. The method was evaluated using 104 PET/CT images collected during cancer screening programs from 2009 to 2012. The sensitivity in detecting candidates at an initial stage was 97.2%, with 72.8 FPs/case. After performing the FP-reduction method, the sensitivity of detection was 90.1%, with 4.9 FPs/case; the proposed method eliminated approximately half the FPs existing in the previous study.

Setio et al. [37] developed a novel Computer-aided Diagnosis (CAD) system for pulmonary nodules using Multi-view Convolutional Networks (ConvNets). The network is fed with nodule candidates obtained by combining three candidate detectors specifically designed for solid, subsolid, and large nodules. For each candidate, a set of 2D patches from differently oriented planes is extracted. The proposed architecture comprises multiple streams of 2D ConvNets, for which the outputs are combined using a dedicated fusion method. Data augmentation and dropout are applied to avoid overfitting. The method was trained using the available dataset, Lung Image Database Consortium (LIDC-IDRI) that contains 1 018 CT scans. The candidate detection algorithm detects 93.1% nodules at 269.2 FPs/scan, while the method proposed combined with candidate detection achieves a sensitivity of 85.4% and 90.1% at 1 and 4 FPs/scan, respectively.

In Table 3.4, a summary of the FP reduction works are presented.

3.2.2 MRI

Image Segmentation

MRI Segmentation is required to separate all the different organs and tissues present in the image. The methods developed must consider the type of MRI used as T1-W, T2-W, DCE-MRI, since that for each image a different processing approach may be applied.

Tian et al. [38] developed a supervoxel based segmentation method for prostate MRI. The

Table 3.4: Main topics of the research projects related to FP reduction.

Authors	Target Tissue	Dataset	Evaluation Metrics	Results
Teramoto et al. [36]	Pulmonary Nodules	140 PET/CT collected from 2009 to 2012	Sensitivity, FPs	97.2%, 72.8 FPs/case decreased to 90.1%, 4.9 FPs/case
Setio et al. [37]	Pulmonary Nodules	1.018 CT scans from acrshortlidc	Sensitivity, FPs	93.1%, 269.2 FPs/scan decreased to 85.4%, 90.1% to 1, 4 FPs/case

prostate segmentation problem was considered a binary problem with two classes: prostate and background. The proposed approach consists of three parts: supervoxel generation, graph cuts and 3D active contour model. After obtaining the supervoxel using SLIC, a neighborhood system is built by connecting supervoxel to each. The supervoxel labeling problem is considered as a minimization of an energy function by using graph cuts. A supervoxel-based shape data term and a supervoxel-based smoothness term are computed to construct the energy function. Lastly, a 3D active contour model is introduced to refine the segmentation obtained from graph cuts. To evaluate this approach, two databases are used: a DB acquired in-house composed of 30 prostate MRI volumes and the PROMISE12 challenge dataset, which has 50 training images and 30 testing images. All these images are T2-W MRI volumes. The proposed method was evaluated based on four quantitative metrics, which are DSC, Relative Volume Difference (RVD), HD, and Average Surface Distance (ASD). The proposed method achieves for the in-house dataset 87.19±2.34% of DSC, -4.58% of RVD, 9.92±1.84 mm of HD and 2.07±0.35 mm of ASD and for the PROMISE12 challenge dataset 88.15±2.80% of DSC, 2.82 of RVD, 5.81±2.01 mm of HD and 2.72±0.77 mm of ASD. These values show that the proposed method has a high accuracy and robustness and can segment the prostate with a small error.

Pereira et al. [39] proposed an automatic segmentation method based on CNN, exploring small 3x3 kernels. The method was validated in the Brain Tumor Segmentation Challenge 2013 Database (BRATS). For each patient in BRATS, there are four MRI sequences available: T1-W, T1 with gadolinium enhancing contrast, T2-W and FLAIR. The training set of BRATS 2013 contains 20 High Grade Gliomas (HGG) and 10 Low Grade Gliomas (LGG), with manual segmentations available. Two testing sets are available in this DB: Leaderboard composed by 21 HGG and 4 LGG and the Challenge set that includes 10 HGG. This problem was considered as a multi-class classification problem with 5 classes (normal tissue, necrosis, edema, non-enhancing, and enhancing tumor). This method achieved for the Leaderboard data set for the classes complete, core and enhancing regions the values of 0.84, 0.72 and 0.62 in DSC, 0.85, 0.82 and 0.60 in PPV and 0.86, 0.76 and 0.68 in Sensitivity and for the Challenge dataset the value of 0.88, 0.83 and 0.77 in DSC, 0.88, 0.87 and 0.74 in PPV and 0.89, 0.83 and 0.81 in Sensitivity,

respectively.

In Table 3.5, a summary of the topics of the works of MRI segmentation are presented.

Table 3.5: Main topics of the research projects related to MRI Segmentation.

Authors	Target Tissue	Dataset	Evaluation Metrics	Results
Tian et al. [38]	6 fragments: brain, bladder, heart, left and right kidneys and other hypermetabolic	BRATS 2013 dataset: training 20 HGG and 10 LGG; Leaderboard 21 HGG and 4 LGG; Challenge 10 HGG	DSC, PPV, Sensitivity	Leaderboard: 0.62-0.84,0.60-0.85,0.68-0.86 Challenge:0.77-0.88,0.74-0.88,0.81-0.89
Pereira et al. [39]	Prostate	30 prostate MRI volumes and the PROMISE12 challenge dataset (50 training and 30 testing images)	DSC, RVD, HD, ASD	For first dataset: 87.19±2.34%,-4.58% 9.92±1.84 mm and 2.07±0.35 mm For PROMISE12 dataset: 88.15±2.80%, 2.82%,5.81±2.01 mm and 2.72±0.77 mm

Chapter 4

Experimental Setup

In this chapter, the several steps of the adopted approach are described, from the data collection, the analysis of PET/CT to the analysis of MRI. A diagram of these steps is represented in Figure 4.1.

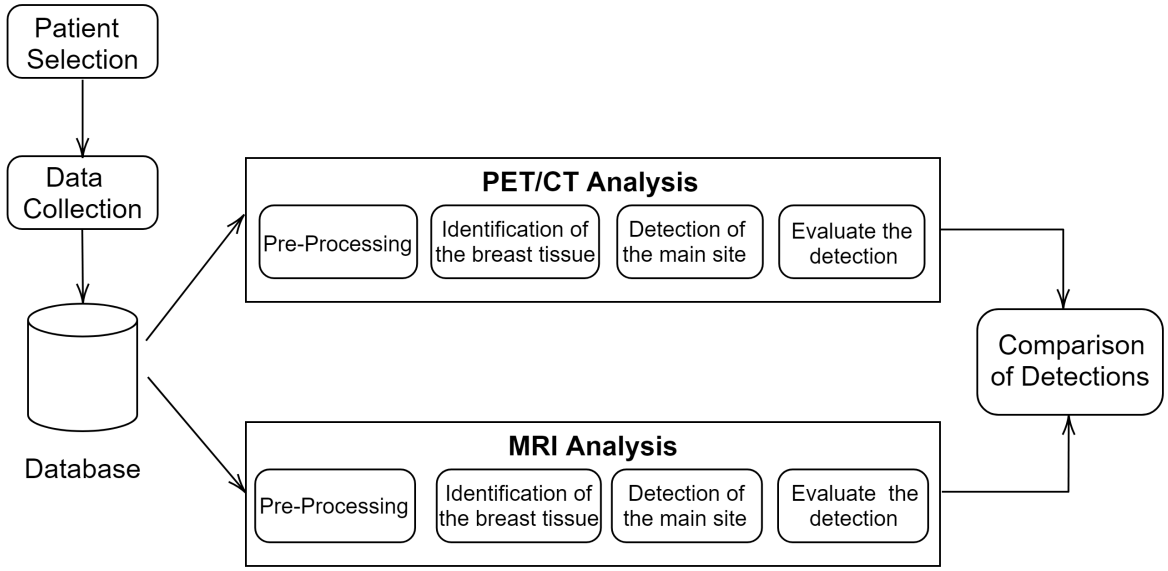

Figure 4.1: Diagram of the various steps constituting the methodology.

4.1 Data Collection

The first step developed was the data collection at IPO Porto. This phase was a very time consuming lasting 4 months, which required a lot of time reviewing clinical cases and collecting images as well as medical reports.

A list of 593 patients was selected from the period between the years 2013 and 2018 that

performed PET/CT and were diagnosed with BC. This list was filtered by the Director of the Nuclear Medicine Service, eliminating all the cases in which BC was not the primary tumor and the PET/CT imaging exam was not used for staging purposes. In total, 342 patients were included in this study.

After patient selection, the imaging exams performed for each patient during the staging phase were collected with the corresponding medical report.

To access this data, three information systems had to be manually accessed for each patient: one system contains the clinical information, other system stores the medical images in DICOM format and the last system organizes the medical reports.

Each patient is associated with a patient ID, however in the data processing phase, this value was masked for data protection reasons.

4.1.1 Data Organization

The collected Data is composed by several imaging modalities, such as: PET/CT, MRI, Bone Scintigraphies, Breast or Axillary Echographies/Ultrasound Scans, Mammographies and Thorax CT Scans.

During the staging process, not all mentioned modalities are performed for all patients because the resulting imaging might not be necessary to acquire the clinical information necessary to define the stage of the disease and choose the treatment. Due to this fact, not all modalities defined to constitute this Database (DB) exist for each patient and a few modalities may have been repeated. This required a revision of the exams and a selection of the exam to include. The final representation of each modality in the collected DB is presented in Table 4.1.

Table 4.1: Representation of each Modality in the collected Database.

Modality	**Number of patients**
PET/CT	342
MRI	155
Bone Scintigraphy	195
Ecography	268
Mammography	230
Thorax CT Scan	106

4.1.2 Subset of Data Selected

In the development of this work, two modalities were considered to compare with PET/CT: MRI and Bone Scintigraphy. Both modalities were highlighted because MRI can diagnose local and regional nodules and Bone Scintigraphy can diagnose bone metastases, while the other modalities can detect lesions in only one area. However, due to time restrictions, only a modality

could be chosen. This decision took in consideration the representation of each modality in the DB, as well as the relevance of the results obtained through the imaging analysis.

In order to compare the detection between PET/CT and Bone Scintigraphy, it was required that most of the patients had to be positive for bone metastases. However this does not happen, because most of the Bone Scintigraphy collected are negative to metastases (70%). Due to this fact, we decided to compare PET/CT and MRI.

To perform that comparison, the patients selected for this study had to follow a few inclusion criteria, such as:

1. Patients performed PET/CT and MRI;
2. Cases where images were acquired in an interval smaller than 6 months apart, the limit time interval in which the imaging modalities are viable to be compared.

Following these criteria, 143 patients were enrolled in this study. Further detail is presented in what follows.

4.1.3 Subset Characterization

This section presents the conclusions obtained after studying the data and the structure of the images of each modality that are going to be processed in the next phase.

4.1.3.1 PET/CT Components

In PET/CT imagiology protocol, several DICOM files are obtained, which include:

- CT - Computer Tomography;
- PET (AC) - Attenuation Corrected Positron Emission Tomography images;
- PET (NAC) - Non-Attenuation Corrected Positron Emission Tomography images;
- AC_CT - Computer Tomography based Attenuation Correction for PET images;
- Patient Protocol;
- PET Statistics - Statistics of the counting of emission, scattering and transmission;
- Topogram - Full body CT Scan.

CT, PET (AC) and PET (NAC) are 3D images, while Topogram is a 2D scan. AC_CT and PET Statistics are images describing the Attenuation Process and the Statistics of the acquisition of the PET, respectively, while Patient Protocol is a DICOM file with information describing all the protocol of the acquisition of the image.

For each exam, if one of these components is repeated, a manual selection was applied and only the best image or the full body image was selected.

4.1.3.2 MRI Components

Each patient in the DB performs different types of MRI protocols. A MRI protocol is defined by a sequence of specific sequences defined for each patient. Due to this fact, specific MRI sequences that are the most useful and most common in the DB must be selected.

Following the recommendations of a BC clinical expert, the best sequences to analyze and process are:

- T1-Weighted (T1-W) Images;
- T2-Weighted (T2-W) Images;
- T2-W Images with Fat Saturation (FATSAT);
- Diffusion Images;
- Dynamic Images;
- Sagittal Slices.

Most of these sequences are volumes (3D), except for Dynamic Images that are composed by a series of volumes over time (4D) and Sagittal Slices that are slices of a volume (2D).

Even though these sequences are common, not all are performed in all MRI protocols. Due to this fact, the presence of each type of sequence in each exam was analysed, to find which are the most common. The representation of each type of sequence is represented in Table 4.2.

Table 4.2: Components present in each MRI exam in the Subset Database.

MRI sequences	Number of Patients
T1 sequences	143
Diffusion sequences	75
T2 - fatsat	36
T2 sequences	143
Dynamic Studies	5
Sagittal Slices	135

The most common sequences are T1-W and T2-W images. These ponderations will be the ones used in this project.

4.1.3.3 Ground Truth Acquisition

The definition of the Ground Truth for PET/CT was performed manually, by comparing the medical reports with the PET images, as described in what follows. Bounding Boxes were defined, isolating areas of hipercaptation and *foci* detected, as illustrated in Figure 4.2.

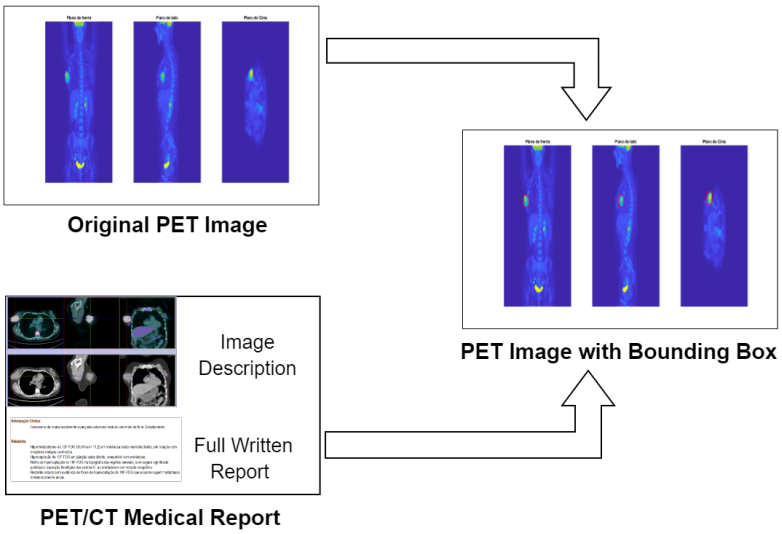

Figure 4.2: Illustration of the PET Ground Truth Acquisitions.

A similar process is applied to MRI. The definition of the Ground Truth for MRI was also performed manually, comparing the written medical reports with the MRI. Bounding Boxes were defined, isolating areas of interest mentioned in the medical reports such as masses and non-mass like enhancements, as illustrated in Figure 4.3. The Ground Truth was defined in T1-W images, considering the reports and images of all T1-W, T2-W and Contrast-Enhanced images. It was necessary to analyse all these images due to the different tissue characteristics of the various lesions, as illustrated in Figure 4.4. To compare the Ground Truth to T2-W images, T2-W is co-registered (full details are given in Section 4.3.1).

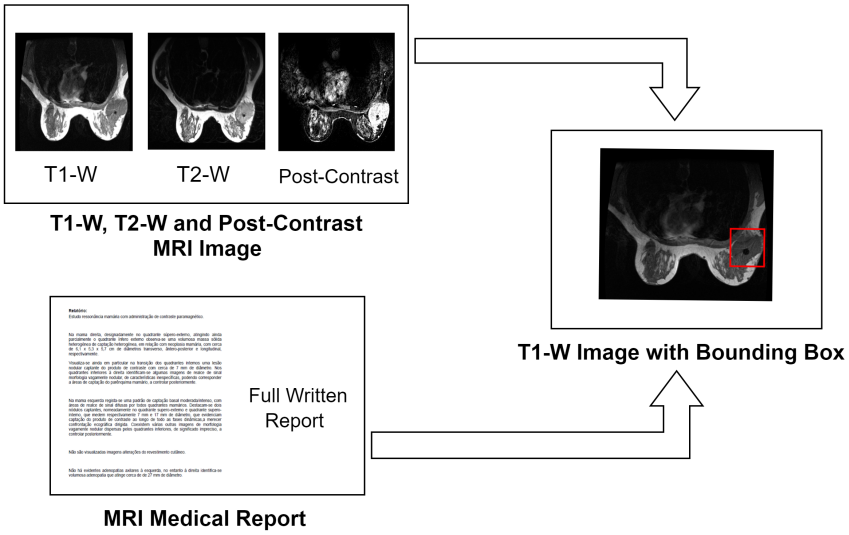

Figure 4.3: Illustration of the MRI Ground Truth Acquisitions.

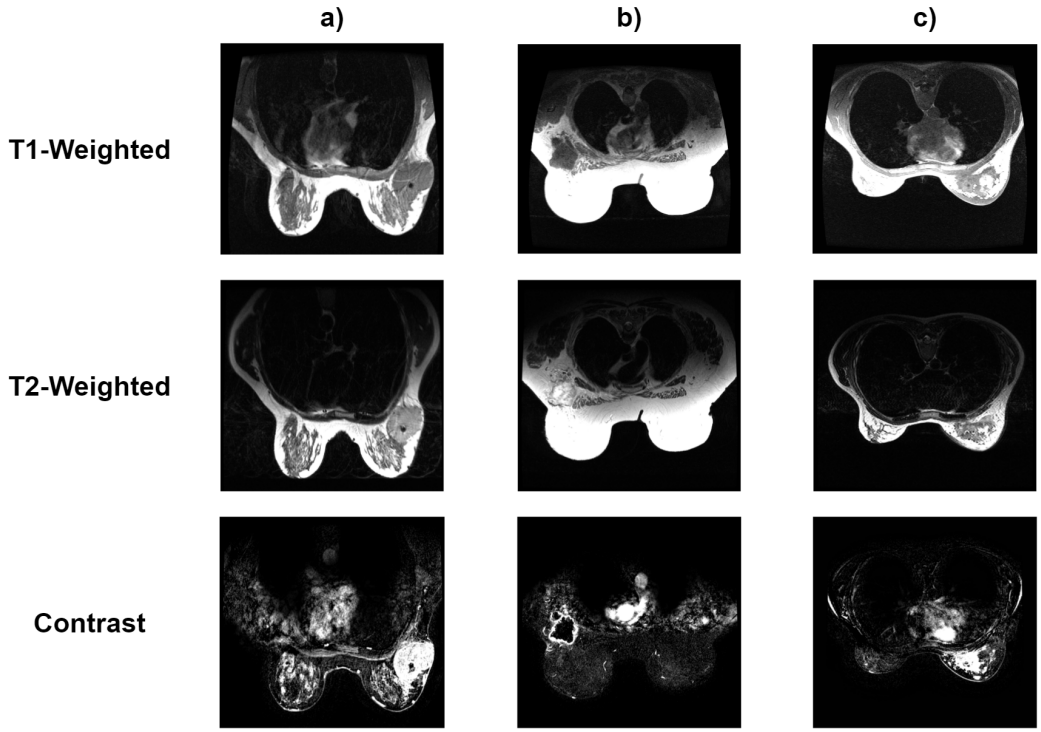

Figure 4.4: Illustration of different tissue signal characteristics in T1-Weighted, T2-Weighted and Contrast-Enhanced MRI: in a), the lesion presents hyposignal on T1-W, hypersignal on T2-W and is enhanced by contrast; in b), the lesion presents isossignal on T1-W, hypersignal on T2-W and is not enhanced by contrast; and in c), the lesion presents isossignal on T1-W and T2-W and is enhanced by contrast.

Since the imaging modalities were acquired within some time difference, the Ground Truth is not the same. From the 143 patients, 132 patients present a Tumor in PET/CT and 140 patients present a Tumor in MRI.

4.2 Analysis of PET/CT

In this section, the steps to analyze the PET/CT images are described. This process is mainly divided into: Pre-processing, Identification of the Breast and Lesion Detection. The complete process is illustrated in Figure 4.5.

4.2.1 Pre-Processing

The pre-processing step reads each DICOM file, builds the PET (AC) volume and the corresponding DICOM header for each slice.

Firstly, all the files in the directory given as input are enumerated. Each file is considered a slice and will be read and placed in the final matrix one at a time.

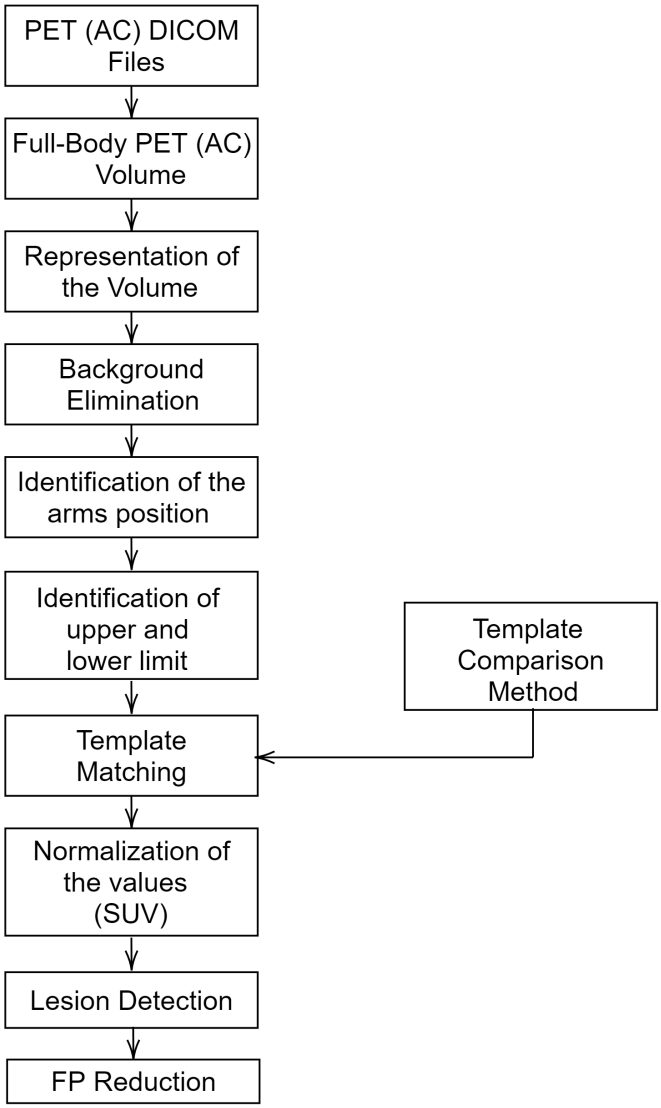

Figure 4.5: Diagram of the Analysis of PET/CT.

Before reading the image from the DICOM file, the information is read and stored in a structure. This information is required to understand how the image is formatted and how the volume should be constructed. After the information is read, each slice is placed in the volume accordingly to the *InstanceNumber* parameter. When the image is stored in the matrix of the volume, a conversion from the stored units to image units is required. The units stored in the DICOM format do not correspond to the PET units, in this case, Becquerels/Millimeter (BQML), because the meaningful units are not necessarily the most convenient or efficient to use in a storing format. The conversion is applied according to equation 4.1.

$$Value\ PET(AC)\ volume = Raw\ Value * RescaleSlope + RescaleIntercept \quad (4.1)$$

During the creation of the PET volume, a specific position was chosen for all patients, which is illustrated in Figures 4.6 and 4.7, that corresponds to a standing position where the patients are looking forward.

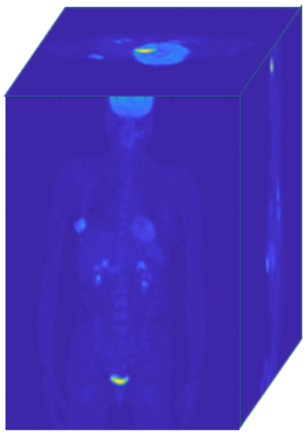

Figure 4.6: Illustration of the final 3D volume in PET.

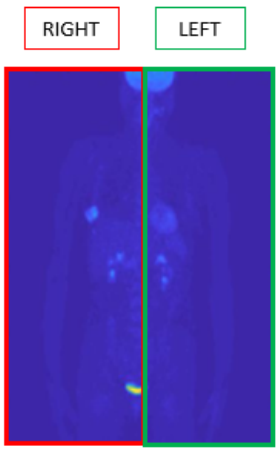

Figure 4.7: Illustration of the right and left side of the body of the patient in PET.

In order to obtain this position, it is required to transpose each slice so that the head of the patient is on the left side of the image. After that rotation, there are a few cases where the patient is not standing up and to verify that condition and invert it if needed, a few parameters must be considered.

The *PatientPosition* specifies the body position of the patient in relation to the PET scanner. For the data in the DB, there are two possible values: Head First-Supine (HFS) and Feet First-Supine (FFS).

After obtaining the position of the body of the patient, it is required to consider the position of each slice accordingly to the reference axis system, which is obtained by the *SliceLocation*.

After all these adjustments, the volume of PET (AC) is ready to be used.

4.2.2 Identification of the breasts

The segmentation of the target volume is the first step to accomplish before applying any type of detection on the image. This process is composed by several segments, each one solving a specific area and using several approaches, which will be explained in what follows. The final result is illustrated in Figure 4.8.

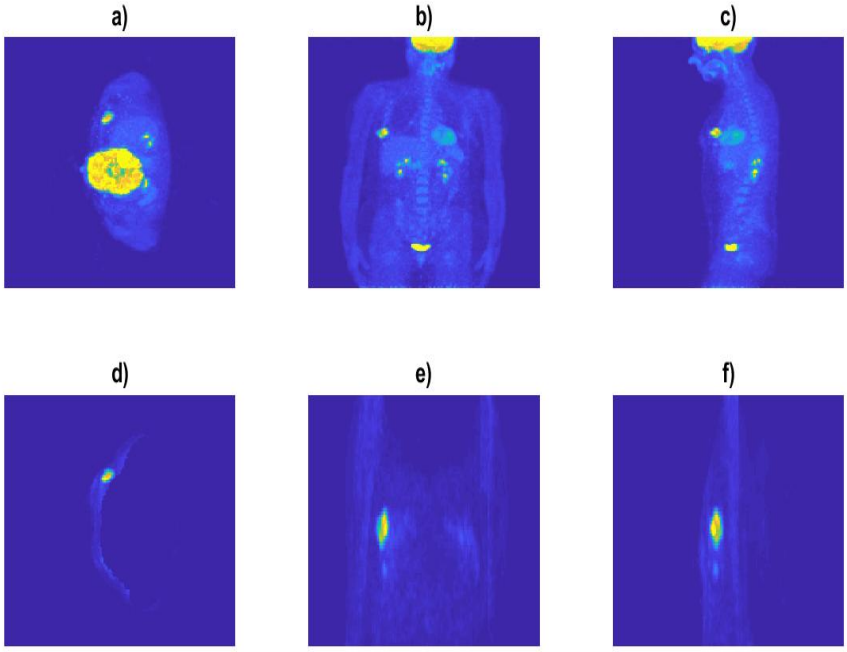

Figure 4.8: Results of the Identification of the breast tissue: a) Top MIP of the full body; b) Frontal MIP of the full body; c) Lateral MIP of the full body; d) Top MIP of the breast tissue; e) Frontal MIP of the breast tissue; and f) Lateral MIP of the breast tissue.

4.2.2.1 Representation of the full volume

To identify the volume, a representation of the image in three 2D planes is used to reduce the complexity of the methods developed. This representation allows the identification of several features common in all images that are essential in the tissue identification phase. Considering the objective of representing the full volume using the projection planes, the MIPs were chosen to represent the body.

4.2.2.2 Background Elimination

The next step is to eliminate the background and identify the contour of the body. In this approach, a fixed threshold was defined to eliminate the background.

After applying the threshold, morphological operations are applied to eliminate small regions and holes in the masks that are going to be used to segment the body, which are the frontal and lateral projections as illustrated in Figure 4.9.

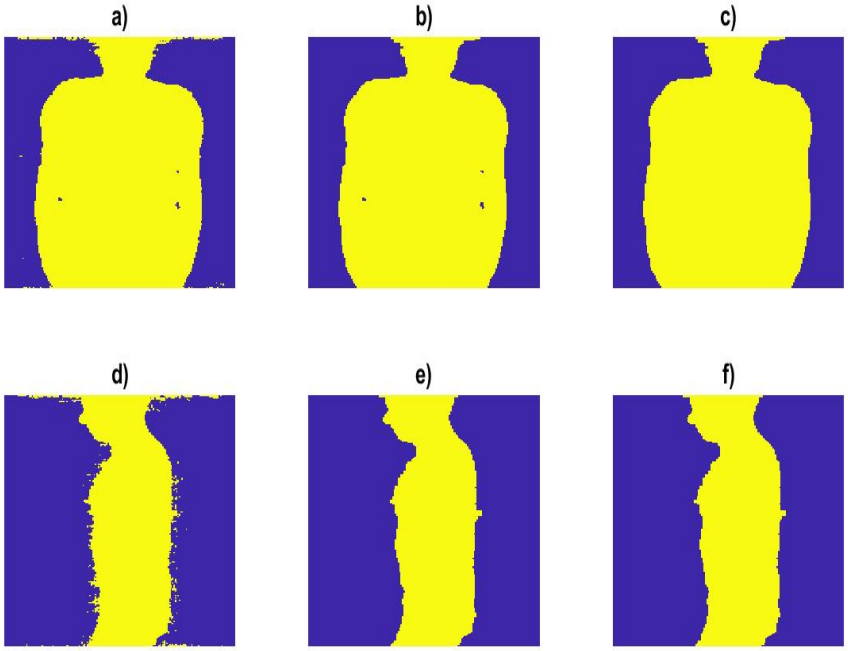

Figure 4.9: Binary Masks obtained from the Frontal and Lateral MIP: a) and d) Applying Threshold; b) and e) Elimination of small regions; and c) and f) Filling Holes.

4.2.2.3 Dividing the different parts of the body

After obtaining the projections, the contour of the body is obtained and that provides enough information for further segmentation. The steps performed were:

- **Identifying Arms Position:** Arms Up or Arms Down

  The arms position can be either with the arms up or with the arms down, as illustrated in Figure 4.10. In order to accomplish this step, the mask originated from the background removal in the frontal projection is used and the values of a line intersecting the head are evaluated.

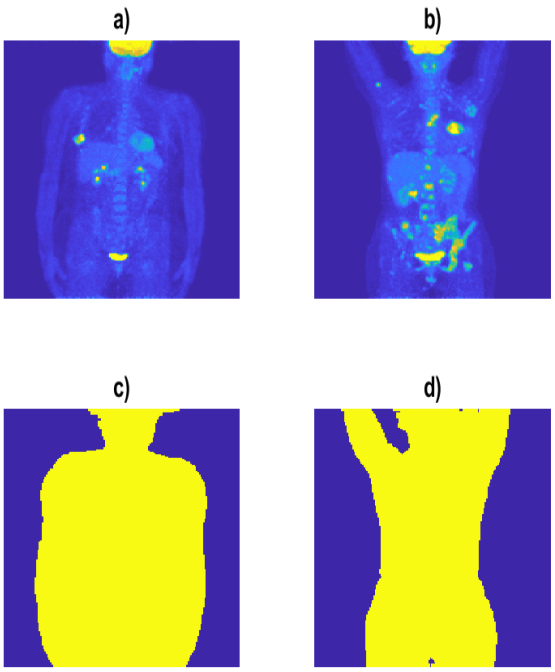

Figure 4.10: Maximum Intensity Projection and Binary Mask obtained from the Frontal Perspective: a) and c) Patient with the arms down; and b) and d) Patient with the arms up.

- **Segment Upper Limit:** Neck Limitation

  To eliminate the head and most of the shoulders' area, the curve of the neck is identified using the contour of the body in the lateral projection, as illustrated in Figure 4.11. The minimum value of the curve corresponding to the neck is identified and this value is considered the upper limitation of the breast volume.

- **Segment Lower Limit:** Breast Curve Limitation

  To define the lower limit, the nipple is identified using the contour of the body in the lateral projection and the fold under the nipple is considered the minimum value after the nipple. The position of the fold under the nipple is defined as the lower limit, as illustrated in Figure 4.12.

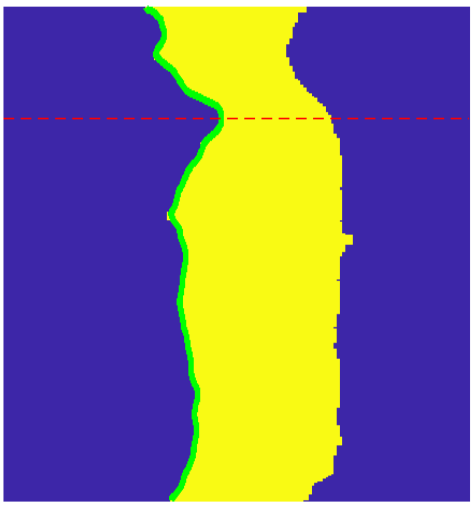

Figure 4.11: Defining the upper limit: green line corresponds to the contour of the body and the red line corresponds to the obtained upper limit.

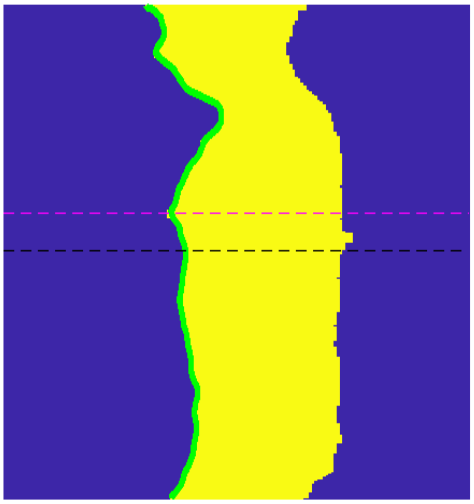

Figure 4.12: Defining the lower limit: green line corresponds to the contour of the body, the pink line corresponds to the nipple level and the black line corresponds to the obtained lower limit.

- **Segment Posterior Limit:** Ribs Limitation / Template Matching

  After defining the volume where the breast tissue is located, it is necessary to eliminate the rib cage volume so that the activity from other organs in that area, such as heart, liver and lungs, does not affect the detection process.

To perform this task, a template matching approach is defined, described in Figure 4.13.

First, two templates of the contour of the breast tissue are created, one for a patient with the arms positioned upwards and another for a patient with the arms positioned downwards. The patients selected to create these templates are chosen from the original DB and do not belong to the subset used in this study. This choice is made in order to preserve the number of patients in the analysis. The templates are obtained using the Computational Environment for Radiological Research (CERR) software and the .mat structures originated are implemented into the code, requiring a few transformations and adaptations [40].

Secondly, for each patient in the subset of the study, a template is chosen according to the patients arms position. After choosing the template, a homogenization of the pixel size and a normalization of the pixel value is performed [9]. The co-registration transformation between the volumes is applied with the source of binary masks and the resulting transformation is applied to the template of the breast volume originating the mask to be applied in the original volume of the Patient.

Finally, the mask is defined and applied to the original volume. In this process, a resizing of the template is required and a MIP of the template is applied into the volume of the breast, isolating the breast tissue from all the rest of the rib cage tissues.

4.2.2.4 Normalization between PET images

In order to compare the images, a normalization of the values is required, due to variability between the images caused by the heterogeneity of the quantity of radiopharmaceutical injected, the weight of the patient and others. To accomplish this step, the most common parameter for PET quantification, Standardized Uptake Value (SUV), was applied.

Even with the applicability that SUV presents for PET interpretation, these values cannot be calculated without the manufacturers' software. In order to obtain the SUV values from PET values, an approach was applied using the most important factors, but ignoring the variability of reconstruction parameters, attenuation parameters, partial volume effect, plasma glucose level in patient blood and the format in which each manufacturer saves the data in DICOM files [41, 42].

The calculation of the value of SUV was based on the equations 4.2, 4.3, 4.4 and 4.5.

$$SUV = \frac{Activity\ Concentration\ (Bq/ml)}{\frac{Injected\ Dose\ (Bq)}{Body\ Weight\ (kg)}} \tag{4.2}$$

$$Activity\ Concentration = Value\ PET(AC)\ volume \tag{4.3}$$

$$Injected\ Dose = Radionuclide\ Total\ Dose * Decay \tag{4.4}$$

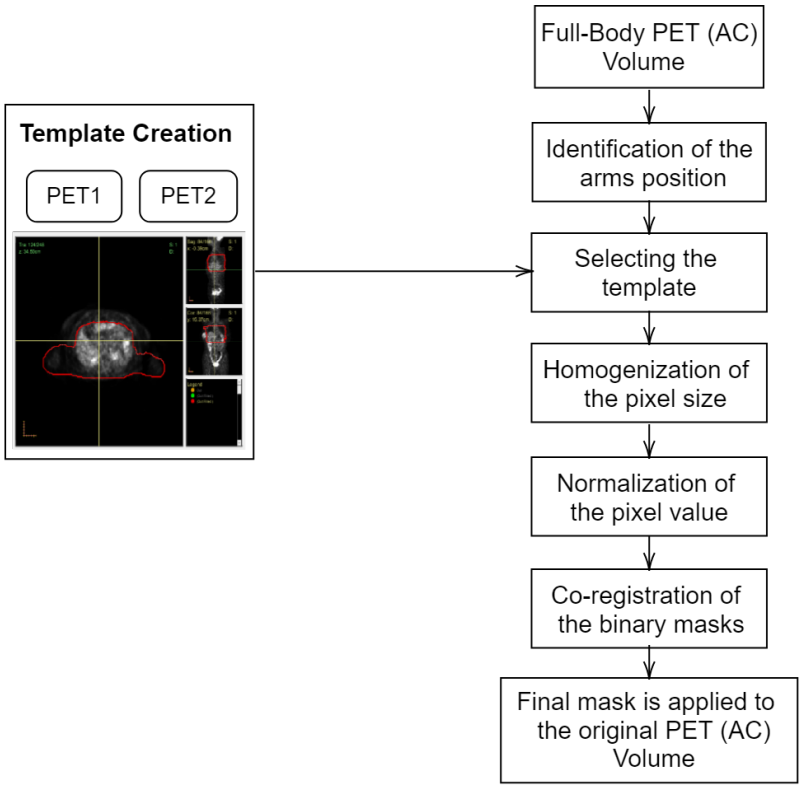

Figure 4.13: Diagram of the Template Matching Method.

$$Decay = e^{-log(2) * \frac{Time\ of\ Acquisition - Time\ of\ Injection}{Radionuclide\ Half\ Life}} \tag{4.5}$$

Even though most of parameters were included in all patients, weight and the time difference between the injection of the dose and the acquisition of the image were absent in a few cases. For these cases, weight was defined as 75 kg and the time difference was considered to be composed by 90 minutes of waiting time and 15 minutes of preparation, which corresponds to the average weight of a woman and the time corresponds to the average time of preparation for acquiring PET/CT images [42].

4.2.3 Lesion Detection

Lesion detection in PET images is based in the implementation of the detection of local maximums that might represent higher values of SUV than the considered metabolically normal. For this stage, it is considered that the values that are higher than 40% are important to be detected, which is the most common value in a clinical setting [43].

SUV values may vary depending on the disease and patient. However, the cut-off value for malignant lesions is 2.5 [41]. Nevertheless, lower values might also be able to detect anomalies

and may be annotated in medical reports. As this work is based in the medical interpretation of the lesions detected, we defined as a minimum SUV value for lesion detection the value of 2.

4.2.4 FP Reduction

The final step of the process consists of the elimination of false detections. After the Lesion Detection phase, there are small detections that cannot be considered a tumor detection due to their dimension. To accomplish this step, a filter was implemented to discard all detections with at least one dimension with only one pixel of length.

4.3 Analysis of MRI

In this section, the steps to analyze the MRI images are described. This process is mainly divided into: Pre-processing, Identification of the Breasts and Lesion Detection (Figure 4.14).

4.3.1 Pre-Processing

The pre-processing phase of MRI reads both T1-W and T2-W DICOM files, builds the MRI volumes, reads the DICOM header for each slice, adjusts the image intensity values and co-registers the T2-W volume considering T1-W volume as the reference.

Firstly, the directory of the files from each volume is given as an input, and the DICOM files are read and placed in the final matrix one by one, accordingly to the *InstanceNumber* parameter. The DICOM header associated to each slice is read and stored into a structure. This information is essential to understand the resolution and dimensions of the image.

The final volumes created respect a specific position chosen for all patients, that corresponds to a standing position where the patients are looking forward, the same position defined for PET images. A illustration of the positioning of the breast tissue is presented in Figures 4.15 and 4.16. The process described to obtain this position in PET images is applied to MRI.

After positioning the body of the patient, the volume is normalized and a transformation is applied to adjust the image intensity values. This transformation saturates the bottom 1% and top 1% of all pixel values, which increases the contrast of the image. This step is performed to reduce inhomogeneities in the voxels intensities across the image and small movement artefacts.

The final step is the co-registration of T2-W volume considering T1-W volume as reference to correct misalignment between the two images. The applied co-registration uses the co-registration of two binary mask and the final result is a T2-W image with the same orientation and size as the T1-W image. The co-registration allows the comparison between the two images as well as the Ground Truth.

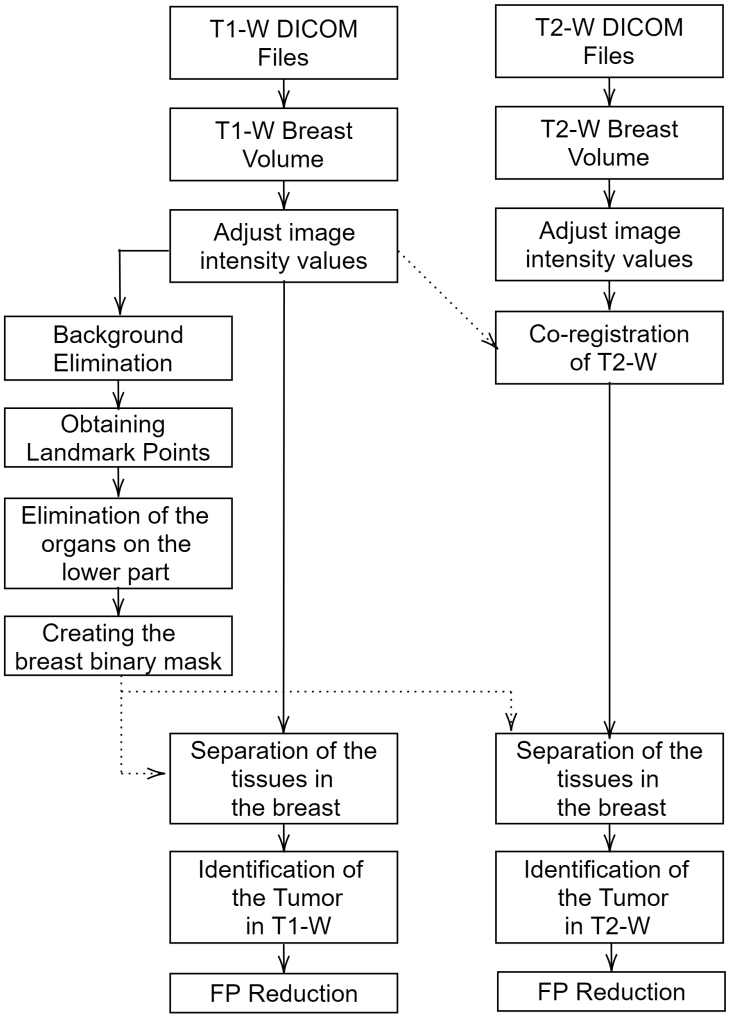

Figure 4.14: Diagram of the Analysis of MRI.

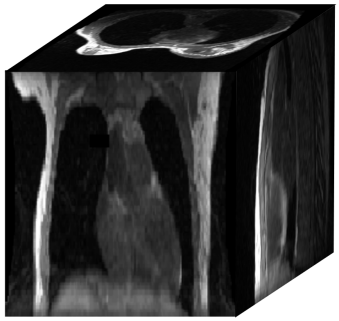

Figure 4.15: Illustration of the final 3D volume in T1-W MRI.

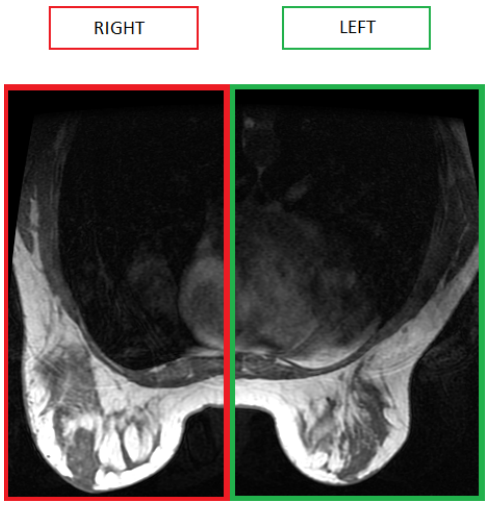

Figure 4.16: Illustration of the right and left side of the body of the patient in T1-W MRI.

4.3.2 Identification of the breasts

The process of the identification of the breast tissue is only performed on T1-W volumes resulting in a binary mask. This step is not repeated on T2-W volumes because the same binary mask can be applied in both volumes. The chosen approach is based on the detection of several anatomical features, performed slice by slice and was inspired by the work of Sehrawat et al. [44]. An illustration of the results of the process is represented in Figure 4.17.

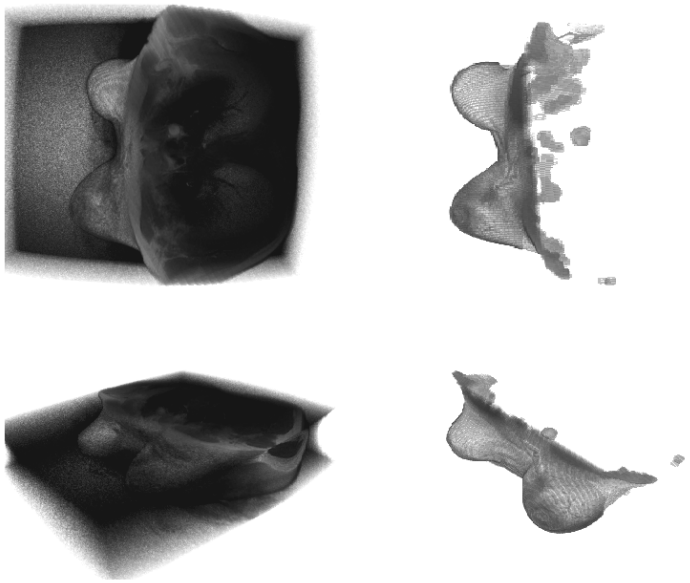

Figure 4.17: Illustration of the results of the identification of the breast tissue. The images on the left are 3D representations of the full image and on the right are a 3D representation of the breast tissue.

4.3.2.1 Background Elimination

The first step consists on the elimination of the background. To perform this step, a fixed threshold is defined and morphological operations are applied to eliminate small regions and holes in the final mask, as illustrated in Figure 4.18.

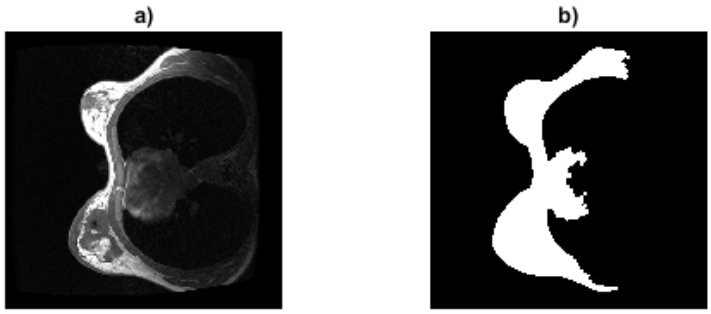

Figure 4.18: Illustration of the Background Elimination in MRI: a) Original Slice; and b) Binary Mask without background.

4.3.2.2 Obtaining Landmark Points

After obtaining the mask without the background, the contour of the body is defined and certain points are identified: the left and right nipples and the middle point between the breasts, as illustrated in Figure 4.19.

The nipples are considered the maximum values of the contour and the middle point is a point in the contour of the body centered between the nipples.

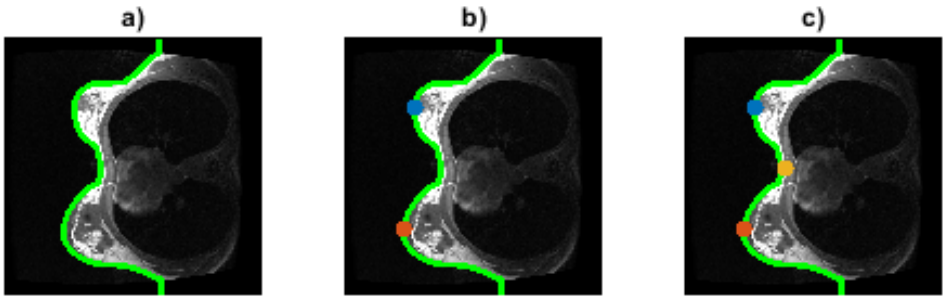

Figure 4.19: Illustration of the Landmark Points Positioning: a) Contour of the body; b) Definition of both nipple positions; and c) Definition of the middle point.

4.3.2.3 Elimination of the organs on the lower part of the breast image

The determination of the localization of the middle point allows the definition of the border between the breast tissue and the inner organs. The area of the organs is separated and is

applied an Otsu's Threshold. Both images are then connected. The steps of this process are illustrated in Figure 4.20

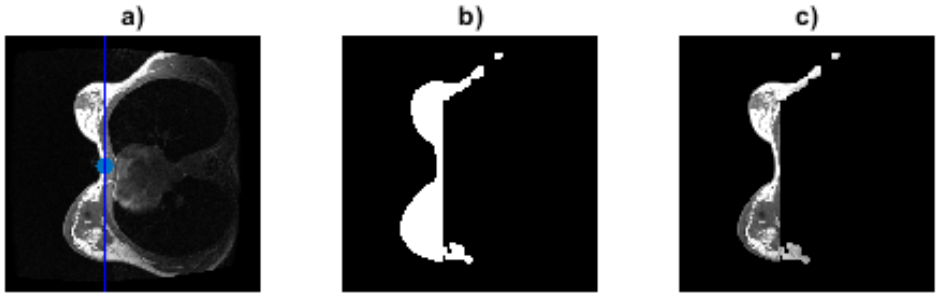

Figure 4.20: Illustration of the elimination of the organs on the lower part of the image: a) Division of the image; b) Mask resulting from the Otsu's Thresholding step; and c) Final segmented image.

4.3.2.4 Creating the breast mask

The final binary mask is a reconstruction of the 2D slices following the process described previously. From the matrix of the binary slices, the biggest connecting volume is selected (eliminating smaller parts outside of the breast volume) and the holes inside the mask are filled. The result is a 3D mask representing the breast volume.

4.3.3 Lesion Detection

Lesion detection in MRI requires primarily a separation of the different breast tissues: Fatty and Fibroglandular Tissue.

To identify the tumor, first it is required to separate these tissues and obtain the Fibroglandular Tissue. Next, segments of tissue that are considered abnormal (tumors) are identified within the Fibroglandular Tissue.

This step is performed separately in the two MRI images (T1-W and T2-W), since the tumor presents different characteristics in each image. Two main image processing techniques are applied: supervoxels and k-means Clustering.

4.3.3.1 Separation of the various tissues in the breast

The first phase of the separation of the various tissues is the extraction of the supervoxels. The binary mask calculated during the identification of the breasts is then applied in order to eliminate the supervoxels that do not belong to the breast.

A matrix of the average values for each supervoxel is calculated, in order to represent the volume. From this step on, this matrix will be used rather than the original volume itself, to take advantage of the supervoxels computation.

After this, K-means Clustering is applied to the average matrix to create three main clusters: Background, Fibroglandular Tissue and Fatty Tissue.

All the described process is illustrated in Figure 4.21.

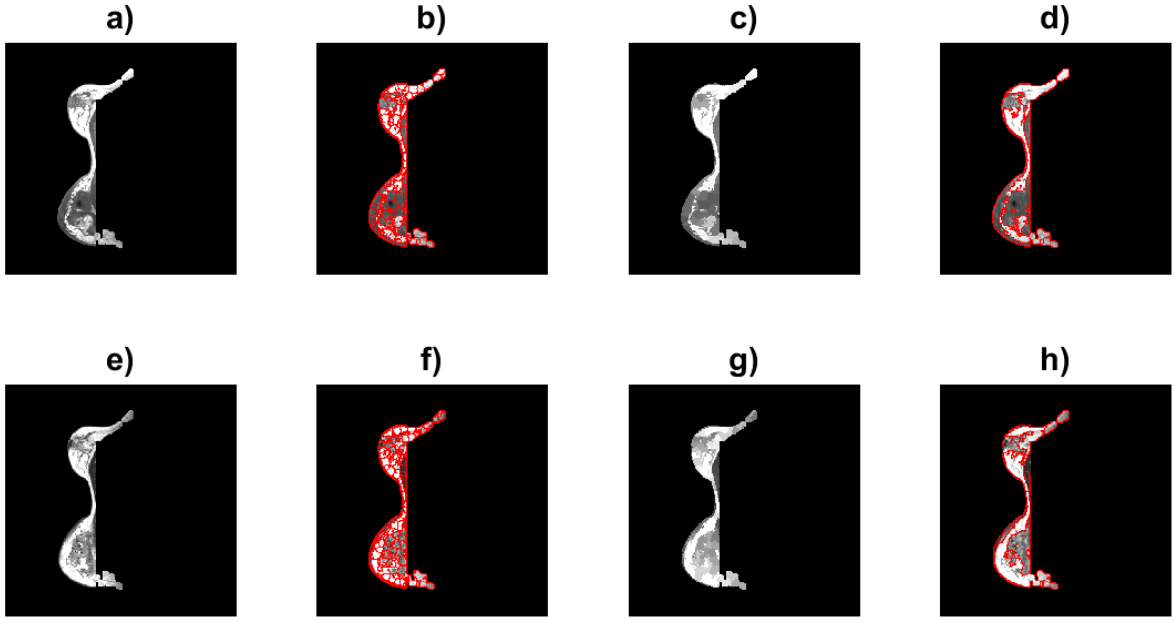

Figure 4.21: Illustration of the separation between the tissues in the breast. Images in the top are from T1-W images and images in the bottom are from T2-W images: a) and e) Original Slice; b) and f) Supervoxels; c) and g) Average Matrix; and d) and h) Clusters from the K-means Clustering.

The selection of the Fibroglandular Tissue cluster is performed by elimination, because the Background cluster is the cluster with the lowest average and the Fatty Tissue cluster is the cluster with the highest average, illustrated in Figure 4.22.

4.3.3.2 Identification of the tumor in the breast and FP reduction

The identification of the tumor is a step that implements the same image processing techniques presented previously but with a different approach.

Using the Fibroglandular Tissue obtained from the cluster and the Average Matrix, a K-means Clustering is performed again and four clusters are defined: Background, Normal Tissue, Tumor and a remaining part from the Fatty Tissue. This division is implemented in order to eliminate the remaining Fatty Tissue in T1-W. In T2-W, the separation of the tissues eliminates all the remaining tissue.

To select the Tumor cluster in T1-W images, the cluster chosen is the second cluster with lowest average overall. This is due to the fact that the tumor in T1-W presents hyposignal and that corresponds to the second cluster with lowest average overall, since the first corresponds to the Background. To select the Tumor cluster in T2-W images, the clusters chosen are the

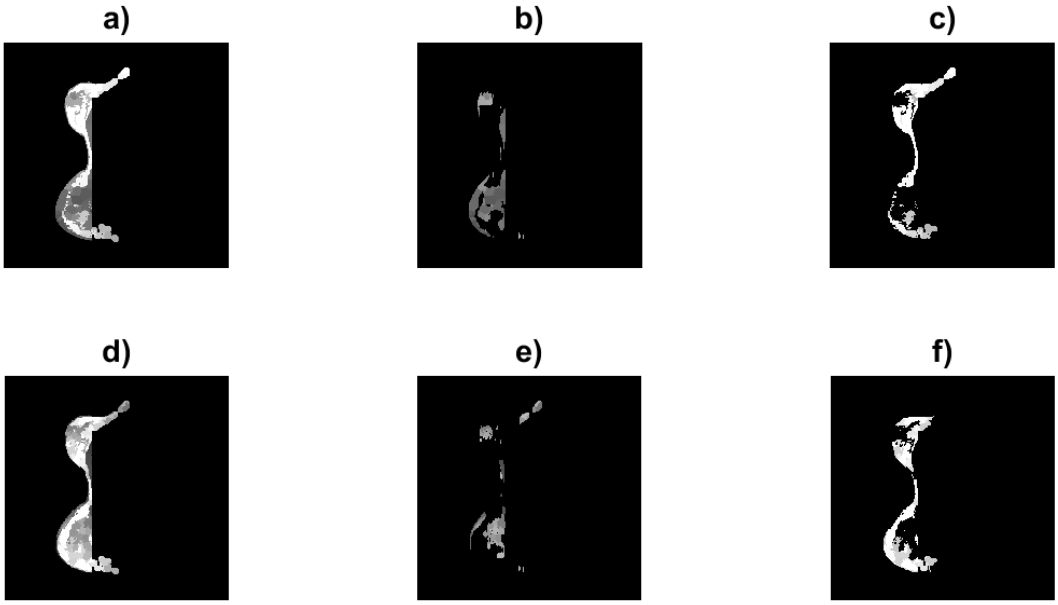

Figure 4.22: Illustration of the separation between the Clusters. Images in the top are from T1-W images and images in the bottom are from T2-W images: a) and d) Average Matrix; b) and e) Fibroglandular Tissue; and c) and f) Fatty Tissue.

second and third with the lowest average overall. This assumption is defined due to the fact that the cluster with lowest is the Background and that in T2-W there is no remaining Fatty Tissue and the tumor is composed by these two clusters. A illustration of this process is represented in Figure 4.23.

The method applied to MRI to reduce the number of FP is the same as described in Section 4.2.4.

4.4 Challenges in the Development of the Algorithms

Throughout the development of this work, several challenges arised due to the imaging modalities used, the resolution and the information obtained from the images and how the chosen algorithms performed for all patients. During this process, all these factors were taken into account and the algorithms presented in Sections 4.2 and 4.3 are the culmination of the best approaches found for each of the problems.

4.4.1 Main Challenges in PET

PET images have very low spatial resolution which increases the difficulty to identify anatomical structures. Even though that process is complex *per se*, a few other problems must be addressed due to the lack of standardization in the imaging acquisition protocol.

The image used in this project is PET (AC) image, extracted from a PET/CT image. During

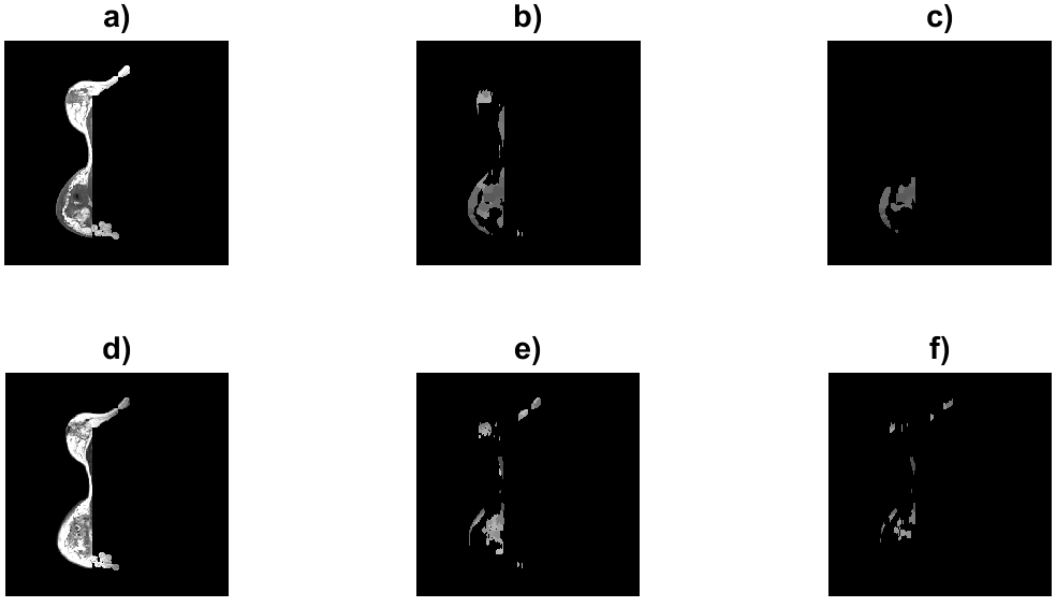

Figure 4.23: Illustration of the identification of the Tumor Cluster. Images in the top are from T1-W images and images in the bottom are from T2-W images: a) and d) Average Matrix; b) and e) Fibroglandular Tissue; and c) and f) Tumor Tissue.

the development of the segmentation algorithm, the CT image was not used to ease this task that requires higher spatial, because the PET used is already corrected accordingly to the CT.

To work with PET images, the 3D image was transformed into 2D projections to ease the extraction of the contour of the body and reduce the complexity of the developed methods. The projection used was the MIP, however other approaches were studied such as average projection and a slice of the volume. These other approaches were useful to detect the upper limit of the volume but failed in the detection of the lower limit, so the MIP was chosen to represent the volume.

Since these images were acquired with different machines and under different conditions, a visual analysis was performed previously to any type of processing, to better understand the types of images obtained and to plan the best methodologies. One of the problems was the position of the arms of each patient caused by the lack of standardization of the position of the patient. To solve this problem, the first step is dedicated to identifying the position of the arms.

The identification of the tissue phase required the definition of the volume in 4 main components: background removal, upper limit, lower limit and rib limitations. The first three steps were performed with simple methods, however the last step was difficult to achieve. The correct delimitation of this area allows the elimination of the contamination from organs that may present high 18F-FDG uptake, such as heart, lungs and liver. To perform this step a few approaches were studied, such as dividing the torso into two parts, interpolating a straight line or a curve between the center of the breast and the axilla, and the template matching approach.

After testing all these methods, the template matching approach achieved the best results.

The detection of the tumor required an additional effort to define the best threshold values to use as well as the cut-off value for malignant lesions. Before considering the implementation of a threshold to identify the peaks of SUV values, a local maximum method was tested. Comparing the values between these methods, the threshold approach was chosen.

4.4.2 Main Challenges in MRI

In MRI, the main challenges found was the understanding of the information provided by the image and the development of the methods to detect the lesions.

As described in Section 4.1.3.3 and illustrated in Figure 4.4, different lesions have different tissue signal characteristics in each image. To separate the tumor from normal tissues, the images were taken into consideration and a few characteristics were noticed:

- The tumor presents hyposignal in T1-W;
- The tumor presents hypersignal in T2-W;
- If the tumor presents isossignal in both T1-W and T2-W, the lesion is only visible in other MRI sequences.

After analysing the images and defining the corresponding Ground Truth, it was possible to verify that only a small percentage of lesions were visually identifiable through T1-W and T2-W images. This is due to the diverse types of existing lesions and can cause a poor detection rate of the lesions.

The identification of the characteristics presented above allowed the establishment of rules to detect the tumor: in T1-W, the detection of hyposignal and in T2-W, the detection of hypersignal.

Before applying the method described to identify the Tumor Tissue in the Fibroglandular Tissue, a threshold technique was performed. However, this method failed due to the value chosen and the presence of Fatty Tissue contaminating the Fibroglandular Tissue. An alternative method using Clustering of supervoxels was implemented and presented better results, and as a result was the approach defined to perform the task.

4.5 Experimental Results

This section is divided into PET and MRI, and an analysis is performed to compare the effects of the FP reduction method.

In order to analyse the efficiency of the algorithms, an evaluation of the matches between the Ground Truth and the Detection is performed, comparing results without and with FP reduction. A match is achieved if Ground Truth and Detection are positive (presence of a tumor) or if

Ground Truth and Detection are negative (absence of a tumor), as explained in Section 2.3.2. The match does not quantify the number of tumors that exist or were detect by the algorithm, instead it verifies if the algorithm is capable to distinguish healthy patients. The calculation of the metrics requires the comparison of bounding boxes. The non existence of a bounding box in Detection or in the Ground Truth makes the calculation of those values impossible. Due to this fact, the metrics are only calculated for cases in which there is a Positive Ground Truth and a Positive Detection.

4.5.1 PET Results

The analysis of the matches presented in Table 4.3, suggests that the method before FP reduction is capable of identifying the cases with positive Ground Truth, only missing 1.4% of the total cases. However, the same cannot be verified for negative cases of Ground Truth, since 5 of the patients without disease are considered FPs.

The application of the method to reduce FP achieves similar results, but the number of cases with positive Ground Truth increase the detection error to 2.8% of the total cases.

Table 4.3: Representation of the Matches in the PET approach without/with FP reduction.

		Detection	
		P	**N**
Ground Truth	**P**	130 / 128	2 / 4
	N	5 / 5	6 / 6

Table 4.4: Evaluation Metrics Values in the PET approach without/with FP reduction.

Evaluation Metrics	**PET approach**
IOU (Approach 1)	0.274/**0.278**
IOU (Approach 2)	0.303/**0.308**
TP per Patient	0.639/**0.648**
FP per Patient	4.285/**2.766**
FN per Patient	0.462/**0.453**
Precision Average	0.325/**0.371**
Recall Average	0.559/**0.568**
Minimal Distance Between Centroids Average	**31.592**/32.982

The description of the metrics of PET approach are presented in Table 4.4. The overall analysis of these values indicates that the approach associated with the FP reduction presents

better results. This approach achieves a IOU of 0.308, a precision of 0.371, a recall of 0.568 and 2.766 FP per patient. Although the results are not ideal, the developed approach seems a promising line for future research.

As a remark, Minimal Distance Between Centroids Average increases after FP reduction, which is due to the fact that the elimination of certain FP bounding boxes increases the distance metric, since the distance between centroids may consider centroids that are not a match.

4.5.2 MRI Results

Besides comparing the results from the approach for T1-W and T2-W images separately, an evaluation is performed by joining the Detection bounding boxes of the two methods. This approach has the objective of evaluating the benefits of aggregating the results of both images.

By analysing the matches described in Table 4.5, it is possible to verify that the application of the FP reduction does not change the values. However, in all approaches, the method cannot identify cases in which no tumour is present. This affirmation cannot be a global conclusion because the DB has a small representation of cases in which the patients have no lesions (only 3 patients).

Table 4.5: Representation of the Matches in the MRI approach without/with FP reduction.

		Detection					
		T1-W MRI		**T2-W MRI**		**T1-W + T2-W**	
		P	**N**	**P**	**N**	**P**	**N**
Ground	**P**	139/139	1/1	140/140	0/0	140/140	0/0
Truth	**N**	3/3	0/0	3/3	0/0	3/3	0/0

The description of the metrics of MRI approach are presented in Table 4.6. Comparing the values from the different MRI types, the best results are from T1-W combined with T2-W MRI without FP-reduction, quantified by the high value of IOU, the highest values of Precision and Recall and the lowest value of FP per patient. The best approach achieves IOU of 0.173, Precision of 0.007, a recall of 0.394 and 22.458 FP per patient.

The same comment in PET related to the Minimal Distance Between Centroids Average, is verified in MRI.

Considering the Table 4.6, it is possible to verify that even though the quantification of matches is equal for the methods without/with FP reduction, the values of the metrics vary between the methods. This conclusion is possible since the matches quantify the existence (or not) of tumor in the Ground Truth or the possibility of the tumor being detected, however they do not quantify the number of lesions. If the method with FP reduction eliminates certain detections, it may not delete the detections that match the Ground Truth and this phenomenon improves the values of metrics such as IOU, Precision, Recall and FP per patient. Overall, the

Table 4.6: Evaluation Metrics Values for MRI without/with FP reduction.

Evaluation Metrics	T1-W MRI	T2-W MRI	T1-W + T2-W
IOU (Approach 1)	**0.099**/**0.137**	0.062/0.083	0.074/0.117
IOU (Approach 2)	0.144/0.143	0.118/0.111	**0.173**/**0.170**
TP per Patient	0.374/0.374	0.250/0.236	**0.443**/**0.436**
FP per Patient	47.273/18.201	**21.121**/**12.400**	68.236/30.643
FN per Patient	0.684/0.684	0.800/0.814	**0.643**/**0.650**
Precision Average	0.009/**0.032**	**0.012**/0.021	0.007/0.016
Recall Average	0.343/0.343	0.223/0.208	**0.394**/**0.387**
Minimal Distance Between Centroids Average	30.245/35.884	30.963/35.523	**22.458**/**26.682**

analyses of the matches is a global approach and is not enough to quantify if the developed algorithm works in patient by patient approach.

4.5.3 Comparing PET with MRI

Comparing the matches and evaluation metrics from both modalities in a general evaluation, it can be seen that the PET approach retrives the best results. However, to further explore this evaluation, the results of the approach of PET with FP reduction and the combination of T1-W and T2-W with FP reduction are going to be compared in more detail.

Focusing on the number of matches between the two approaches, the MRI approach presents better results since it does not have any FN (all patients with disease are identified). However, the same does not occur in PET, since four patients with the disease are considered healthy. The analyses of the matches exemplifies the results between the two approaches, but cannot be considered to achieve a conclusion, the DB is highly imbalanced with a bigger prevalence of cancer cases.

To comprehend how the algorithms perform in a patient by patient approach, an analysis focused on the metrics is required to evaluate the number of tumors correctly identified or the quantity of tumors not detected. Since both algorithms identify different patients as cases of TP for the existence of the disease, only the patients considered TP for the two imaging modalities are considered for this analysis. In total, 127 patients are selected for this analysis. The number of TP, FP and FN varies between modalities, as explained in Section 4.1.3.3, so the metrics of precision and recall are the most appropriate to compare the modalities since they describe the fraction of the numbers.

Based on Precision, the PET approach is able to identify relevant objects better than the

MRI approach in 75 patients, while the MRI is only able to perform better in 18 patients. The other 34 patients considered present the same value of Precision in both modalities (Precision = 0) and correspond to the cases in which neither PET or MRI was capable of detecting any tumor. Based on Recall, the PET approach is able to identify all the correct detections of Ground Truth objects better than the MRI approach in 40 patients, while the MRI is only able to perform better in 20 patients. The remaining 67 patients present the same value of Recall in both modalities and are divided into two groups: 33 patients present maximum value of Recall (Recall =1) and correspond to cases in which both algorithms were able to detect all the TP lesions; 34 patients present minimum value of Recall (Recall = 0) and correspond to cases in which both algorithms were unable to detect any lesions.

This patient by patient analysis allows to verify that in the 127 patients, both algorithms detect correctly the number of tumors in 26.0% of the patients and fail the detection of any tumor in 26.8% of the patients. The PET approach achieves better results in 50% more patients in the detection of tumors and achieves lower percentage of FP than the MRI approach.

Chapter 5

Conclusions and Future Work

In this project, an approach that semi-automatically detects the primary lesion of BC in PET/CT images and MRI is implemented. The motivation for the development of this approach was to reduce the time consuming task that is the annotation of lesions in BC.

The lesion detection was applied in PET images and T1-W and T2-W MRI. The pipeline to detect and localize the lesions is a multi-step method, using various image processing techniques from thresholding to supervoxels.

The approach applied to PET with FP reduction achieved the best results of all approaches. This approach achieved a IOU of 0.308, a precision of 0.371, a recall of 0.568 and 2.766 FP per patient.

Even though these results seem promising, future work must be implemented to increase the accuracy of the algorithm and improve the overall performance. In PET, some methods can be explored such as the association of the PET image into the CT image, experimenting new segmentation techniques and the implementation of other methods to detect abnormal uptakes. In MRI, new types of MRI should be analysed to evaluate how these algorithms performed and the implementation of other segmentation techniques in an 3D approximation, instead of a slice by slice method.

Another method that has been implemented in recent years with an alternative approach is the detection of tumors in the co-registered image PET/MRI. This modality connects the benefits of the detection of abnormal FDG uptake values with MRI proprieties.

Bibliography

[1] International Agency for Research on Cancer. `http://gco.iarc.fr/`. Accessed: 2019-07-10.

[2] Rebecca L. Siegel, Kimberly D. Miller, and Ahmedin Jemal. "Cancer Statistics, 2019". *CA: A Cancer Journal for Clinicians*, 69(1):7–34, 01 2019.

[3] Z. Garami, Z. Hascsi, József Varga, Tamas Dinya, M. Tanyi, Ildikó Garai, L. Damjanovich, and László Galuska. "The value of 18-FDG PET/CT in early-stage breast cancer compared to traditional diagnostic modalities with an emphasis on changes in disease stage designation and treatment plan". *European Journal of Surgical Oncology*, 38(1):31–7, 9 2011.

[4] Jean H. Lee, Eric Rosen, and David A. Mankoff. "The Role of Radiotracer Imaging in the Diagnosis and Management of Patients with Breast Cancer: Part 1-Overview, Detection, and Staging". *Journal of Nuclear Medicine*, 50(4):569–81, 05 2009.

[5] Stephen B. Edge, David R. Byrd, Carolyn C. Compton, April G. Fritz, Frederick L. Greene, and Andy Trotti. *AJCC Cancer Staging Manual, 7th edition.* Springer, 2010.

[6] Anna G Sorace, Sara Harvey, Anum Syed, and Thomas E Yankeelov. "Imaging Considerations and Interprofessional Opportunities in the Care of Breast Cancer Patients in the Neoadjuvant Setting". *Semin Oncol Nurs.*, 33(4):425–439, 2017.

[7] Mariana A. Nogueira, Pedro Henriques Abreu, Pedro Martins, Penousal Machado, Hugo Duarte, and João Santos. "An artificial neural networks approach for assessment treatment response in oncological patients using PET/CT images". *BMC Medical Imaging*, 1(17):13 pages, 2017.

[8] Gisèle Pereira. "Deep Learning techniques for the evaluation of response to treatment in Hodgkin Lymphoma". Master's thesis, Faculdade de Ciencias e Tecnologia, Universidade de Coimbra, 2018.

[9] Gisèle Pereira, Inês Domingues, Pedro Martins, Pedro H Abreu, Hugo Duarte, and João Santos. "Registration of CT with PET: a comparison of intensity-based approaches". *International Workshop on Combinatorial Image Analysis*, pages 134–149, 2018.

[10] Mariana A. Nogueira, Pedro Henriques Abreu, Pedro Martins, Penousal Machado, Hugo Duarte, and João Santos. "Image descriptors in radiology images: a systematic review". *Artificial Intelligence Review*, pages 1–29, 2016.

[11] Sandip Basu, Thomas C. Kwee, Suleman Surti, Esma Akin, Don Yoo, and Abass Alavi. "Fundamentals of PET and PET/CT imaging". *Annals of the New York Academy of Sciences*, 1228:1–18, 06 2011.

[12] John V. Frangioni. "New Technologies for Human Cancer Imaging". *Journal of Clinical Oncology*, 26(24):4012–21, 09 2008.

[13] Sandip Basu, Søren Hess, Poul-Erik Braad, Birgitte Olsen, Signe Inglev, and Poul Flemming Høilund-Carlsen. "The basic principles of FDG-PET/CT imaging". *PET Clinics*, 9(4): 355–70, 08 2014.

[14] Timon Hussain and Quyen Nguyen. "Molecular Imaging for Cancer Diagnosis and Surgery". *Advanced Drug Delivery Reviews*, 66:90–100, 09 2013.

[15] Elizabeth Morris and Laura Liberman. *Breast MRI: Diagnosis and Intervention*. Springer, 2005.

[16] Geon-Ho Jahng, Ka-Loh Li, Leif Østergaard, and Fernando Calamante. "Perfusion Magnetic Resonance Imaging: A Comprehensive Update on Principles and Techniques". *Korean Journal of Radiology*, 15(5):554–577, 09 2014.

[17] Olaf Dietrich, Andreas Biffar, Andrea Baur-Melnyk, and Maximilian Reiser. "Technical aspects of MR diffusion imaging of the body". *European Journal of Radiology*, 76(3):314–22, 12 2010.

[18] Dzung L. Pham, Chenyang Xu, and Jerry L. Prince. "Current Methods in Medical Image Segmentation". *Annual Review of Biomedical Engineering*, 2:315–337, 2000.

[19] Radhakrishna Achanta, Appu Shaji, Kevin Smith, Aurélien Lucchi, Pascal Fua, and Sabine Susstrunk. "SLIC Superpixels Compared to State-of-the-Art Superpixel Methods". *IEEE Transactions on Pattern Analysis and Machine Intelligence*, 34(11), 5 2012.

[20] David Arthur and Sergei Vassilvitskii. "K-Means++: The Advantages of Careful Seeding". *Proceedings of the Eighteenth Annual ACM-SIAM Symposium on Discrete Algorithms*, 8: 1027–1035, 01 2007.

[21] Shuran Song and Jianxiong Xiao. "Sliding Shapes for 3D Object Detection in Depth Images". In *ECCV*, pages 634–651, 2014.

[22] Shuang Liu, Mary Salvatore, David F. Yankelevitz, Claudia I. Henschke, and Anthony P. Reeves. "Segmentation of the whole breast from low-dose chest CT images". *Medical Imaging 2015: Computer-Aided Diagnosis*, SPIE 9414, 03 2015.

[23] Kuo Men, Tao Zhang, Xinyuan Chen, Bo Chen, Yu Tang, Shulian Wang, Yexiong Li, and Jianrong Dai. "Fully automatic and robust segmentation of the clinical target volume for radiotherapy of breast cancer using big data and deep learning". *Physica Medica*, 50:13–19, 06 2018.

[24] Yiping Liu, Hui Liu, Zuowei Zhao, Lina Zhang, and Xiang Liu. "A new active contour model-based segmentation approach for accurate extraction of the lesion from breast DCE-MRI". *2013 IEEE International Conference on Image Processing*, pages 1140–1143, 09 2013.

[25] Albert Gubern-Mérida, Michiel Kallenberg, Ritse Mann, Robert Martí, and Nico Karssemeijer. "Breast Segmentation and Density Estimation in Breast MRI: A Fully Automatic Framework". *IEEE Journal of Biomedical and Health informatics*, 19(1):349–57, 01 2015.

[26] Nicholas Tustison, Brian Avants, Philip Cook, Yuanjie Zheng, Alexander Egan, Paul Yushkevich, and James Gee. "N4ITK: improved N3 bias correction". *Medical Imaging, IEEE Transactions on*, 29(6):1310 – 1320, 07 2010.

[27] Xi Liang, Romamohanarao Kotagiri, Helen Frazer, and Qing Yang. "Automated lesion detection in dynamic contrast enhanced magnetic resonance imaging of breast". *SPIE Medical Imaging 2015: Computer-Aided Diagnosis*, SPIE 9414, 03 2015.

[28] Vishwa Parekh and Michael Jacobs. "Integrated radiomic framework for breast cancer and tumor biology using advanced machine learning and multiparametric MRI". *NPJ Breast Cancer*, 3:43, 12 2017.

[29] Michael Spitzer, Stefan Lorkowski, Paul Cullen, Alexander Sczyrba, and Georg Fuellen. "IsoSVM – Distinguishing isoforms and paralogs on the protein level". *BMC Bioinformatics*, 7(1):110, 02 2006.

[30] Natalia Antropova, Hiroyuki Abe, and Maryellen L. Giger. "Use of clinical MRI maximum intensity projections for improved breast lesion classification with deep convolutional neural networks". *Journal of Medical Imaging*, 5(1):014503, 02 2018.

[31] Aboul Ella Hassanien and Tai-Hoon Kim. "MRI Breast cancer diagnosis approach using support vector machine and pulse coupled neural networks". *Journal of Applied Logic - Elsevier*, 10:277–284, 12 2012.

[32] Beatrice Berthon, Christopher Marshall, Mererid Evans, and Emiliano Spezi. "ATLAAS: an automatic decision tree-based learning algorithm for advanced image segmentation in positron emission tomography". *Physics in Medicine and Biology*, 61(13):4855–69, 04 2016.

[33] Saeedeh Afshari, Aicha Bentaieb, and Ghassan Hamarneh. "Automatic Localization of Normal Active Organs in 3D PET Scans". *Computerized Medical Imaging and Graphics*, 70: 111–118, 09 2018.

[34] Lei Bi, Jinman Kim, Ashnil Kumar, Lingfeng Wen, David Dagan Feng Feng, and Michael Fulham. "Automatic detection and classification of regions of FDG uptake in whole-body PET-CT lymphoma studies". *Computerized Medical Imaging and Graphics*, 60:3–10, 09 2017.

[35] Juanjuan Zhao, Guohua Ji, Yan Qiang, Xiaohong Han, Bo Pei, and Zhenghao Shi. "A New Method of Detecting Pulmonary Nodules with PET/CT Based on an Improved Watershed Algorithm". *PLoS One*, 10(4):e0123694, 04 2015.

[36] Atsushi Teramoto, Hiroshi Fujita, Osamu Yamamuro, and Tuneo Tamaki. "Automated detection of pulmonary nodules in PET/CT images: Ensemble false-positive reduction using a convolutional neural network technique". *Medical Physics*, 43(6):2821–2827, 05 2016.

[37] Arnaud Setio, Francesco Ciompi, Geert Litjens, Paul Gerke, Colin Jacobs, Sarah J. van Riel, Mathilde Marie Winkler Wille, Matiullah Naqibullah, Clara I. Sanchez, and Bram van Ginneken. "Pulmonary Nodule Detection in CT Images: False Positive Reduction Using Multi-View Convolutional Networks". *IEEE Transactions on Medical Imaging*, 35(5): 1160–1169, 03 2016.

[38] Zhiqiang Tian, Lizhi Liu, Zhenfeng Zhang, Jianru Xue, and Baowei Fei. "A supervoxel-based segmentation method for prostate MR images". *Medical Physics*, 44(2):558–569, 12 2016.

[39] Sergio Pereira, Adriano Pinto, Victor Alves, and Carlos Silva. "Brain Tumor Segmentation Using Convolutional Neural Networks in MRI Images". *IEEE Transactions on Medical Imaging*, 35(5):1–1, 03 2016.

[40] CERR: Computational Environment for Radiological Research, Version 2.1. `https://github.com/cerr/CERR`. Accessed: 2018-09-19.

[41] Somphob Soongsathitanon, Pawitra Masa-ah, and Malulee Tuntawiroon. "A new Standard Uptake Values (SUV) Calculation based on Pixel Intensity Values". *International Journal Of Mathematics And Computers In Simulation*, 6:26–33, 1 2012.

[42] Radiomics, Version 1.0. `https://github.com/mvallieres/radiomics`. Accessed: 2019-03-04.

[43] Brent Foster, Ulas Bagci, Awais Mansoor, Ziyue Xu, and Daniel Mollura. "A Review on Segmentation of Positron Emission Tomography Images". *Computers in Biology and Medicine*, 50:76–96, 07 2014.

[44] Snekha Sehrawat, Subhajit Chatterjee, Meenakshi Singhal, Rakesh Gupta, and Anup Singh. "Automatic outer and inner breast tissue segmentation using multi-parametric MRI images of breast tumor patients". *PLoS ONE*, 13(1), 01 2018.